

Optical signatures of the coupled spin-mechanics of a levitated magnetic microparticle

Vanessa Wachter,^{1,2} Victor A. S. V. Bittencourt,¹ Shangran Xie,^{1,*} Sanchar Sharma,¹
Nicolas Joly,^{2,1} Philip Russell,¹ Florian Marquardt,^{1,2} and Silvia Viola Kusminski^{1,2}

¹*Max Planck Institute for the Science of Light, Staudtstraße 2, 91058 Erlangen, Germany*

²*Department of Physics, University of Erlangen-Nürnberg, Staudtstraße 7, 91058 Erlangen, Germany*

We propose a platform that combines the fields of cavity optomagnonics and levitated optomechanics in order to control and probe the coupled spin-mechanics of magnetic dielectric particles. We theoretically study the dynamics of a levitated Faraday-active dielectric microsphere serving as an optomagnonic cavity, placed in an external magnetic field and driven by an external laser. We find that the optically driven magnetization dynamics induces angular oscillations of the particle with low associated damping. Further, we show that the magnetization and angular motion dynamics can be probed via the power spectrum of the outgoing light. Namely, the characteristic frequencies attributed to the angular oscillations and the spin dynamics are imprinted in the light spectrum by two main resonance peaks. Additionally, we demonstrate that a ferromagnetic resonance setup with an oscillatory perpendicular magnetic field can enhance the resonance peak corresponding to the spin oscillations and induce fast rotations of the particle around its anisotropy axis.

I. INTRODUCTION

Since the pioneering work of Ashkin [1], trapping dielectric particles by optical forces has found a wide range of applications [2], ranging from sensing ultra weak forces [3–11] and temperature gradients [12–14] to manipulating biological systems [2, 15–19]. Furthermore, dielectric particles levitated in vacuum are highly isolated from environmental noise and decoherence, offering an ideal playground to control the dynamics of micro- and nanoresonators [20–27]. This has brought forth unprecedented performance in cavity and feedback cooling of levitated particle motion [28–33] and the realization of fast rotation in high vacuum [34, 35]. The high degree of isolation also makes levitated particles a key component in many proposals for exploring quantum mechanics with mesoscopic objects [36–42].

Magnetically ordered dielectrics introduce magnetization as an additional degree of freedom to levitated particles. For example, due to conservation of angular momentum, a change in the magnetization of a freely moving body can lead to its mechanical rotation and vice versa – the so called Einstein-de Haas effect [43] and its reciprocal, the Barnett effect [44]. Furthermore, the magnetization couples to the particle orientation, defined by the specific magneto-crystalline anisotropy of the material [45]. These effects are prominent in magnetically levitated systems and can be harnessed for probing mesoscopic quantum mechanics including rotational degrees of freedom, as well as for sensing [46–59].

The magnetization of dielectrics also can couple to light via magneto-optical effects, the best known being

the Faraday effect: the magnetization-induced rotation of the polarization of light. Conversely, light can also induce a small precession of the magnetization (the inverse Faraday effect) [60, 61]. This generally weak coupling can be enhanced by confinement of light inside of the dielectric, which has given rise to the field of (cavity optomagnonics) [62–74]. The combination of optomagnonic effects with levitation provides a novel system within which light, magnetism and angular motion are intertwined.

In this work, we propose a new scheme for optomagnonically controlling and probing the coupled dynamics of levitated magnetic dielectric microparticles. We consider the system depicted in Fig. 1: a spherical dielectric magnet is levitated in the presence of an external static magnetic field. A pump laser drives two internal electromagnetic field modes of the particle, which couple to the magnetization dynamics via the cavity-enhanced optomagnonic coupling. In turn, the magnetization of the particle couples to its angular motion via both magneto-crystalline anisotropy and dissipation of magnons into the lattice. We show that the optically driven magnetization dynamics induce angular oscillations, which exhibit low damping due to the lack of direct dissipation of the angular motion. The driven angular motion is limited in amplitude by the optical quality factor of the particle and the driving power that the system can support. The coupling between magnetization and angular motion can be probed via the power spectrum of the cavity modes, which exhibits two main resonance peaks that can be linked to the angular oscillations and to the spin dynamics. Finally, we study the case of a driven ferromagnetic resonance (FMR) by adding an oscillatory magnetic field perpendicular to the static magnetic field. We show that this configuration can enhance the visibility of the characteristic peaks in the spectrum and can induce, via the magnetization, fast rotations of the particle around its

* Currently at: School of Optics and Photonics, Beijing Institute of Technology, 100081 Beijing, China

anisotropy axis.

The paper is structured as follows. In Sec. II we present the model and derive the corresponding Hamiltonian. In Sec. III we derive the coupled Heisenberg equations of motion with their conserved quantities and discuss the torque generated by the applied laser via the optomagnonic coupling. Sec. IV presents the steady state configurations of the system. In Sec. V we investigate the nonlinear dynamics of the system numerically. Sec. VI is devoted to the computation of the power spectrum of the cavity field fluctuations and the resonance peaks. In Sec. VII we show the effects of an additional driving magnetic field and we discuss some generalizations to the model in Sec. VIII. We draw conclusions and discuss further directions in Sec. IX.

II. MODEL

We consider a Faraday-active dielectric microparticle that is levitated in the presence of an external static magnetic field \mathbf{B}_0 as depicted in Fig. 1. The magnetization of the particle is saturated along \mathbf{B}_0 . The particle supports internal electromagnetic modes. If the radius of the particle is much larger than the driving laser wavelength, light is trapped by total internal reflection, forming optical whispering gallery modes [75]. Otherwise, for radii comparable to the driving light wavelength, such modes correspond to Mie resonances [76, 77]. In case of an unmagnetized particle the underlying Mie mode frequencies are solely determined by the polarization and the angular mode number, and the modes are degenerate with respect to the azimuthal number. The magnetization of the particle breaks this degeneracy and causes a splitting of the Mie modes into modes with different azimuthal numbers [66, 78].

Driving the particle with light can induce a precession of the magnetization around its equilibrium orientation. The associated quantized magnetic excitations are denoted magnons. The mean number of magnons in a coherent state is directly related to the amplitude of the magnetization precession. In the following we focus on the homogeneous magnon mode, known as the Kittel mode, consisting of a uniformly precessing magnetization. Its frequency can be tuned by the external magnetic field and usually lies in the GHz regime. For a driving electromagnetic field at optical frequencies, the resonant dipolar coupling between the magnetization and the magnetic field is suppressed due to the mismatch of frequencies. The coupling to the electromagnetic field takes place instead through a Raman scattering type of process involving two photons, and it is dominated by the dipolar coupling to the *electric component* of the field [79].

In this work, we consider that a pump laser of suitable

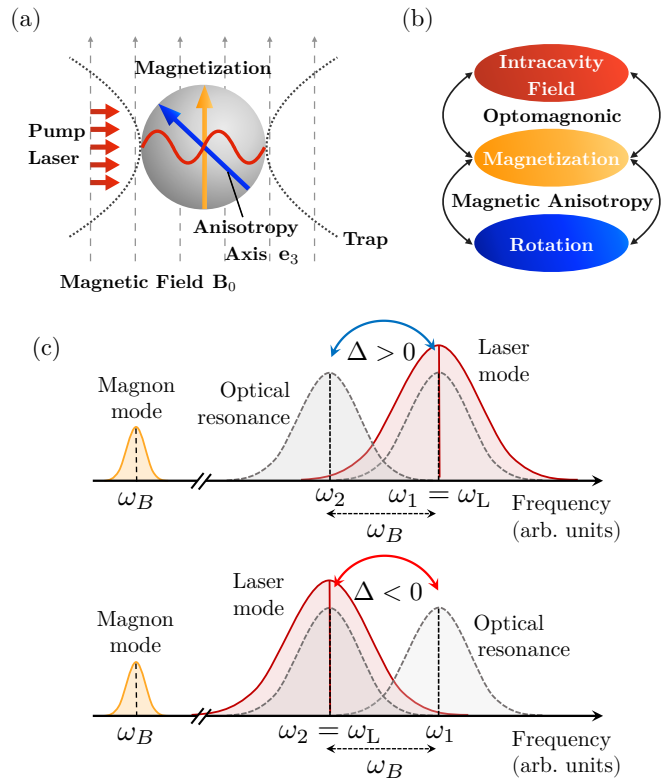


Figure 1. Schematic of the model, showing the couplings between the relevant degrees of freedom. (a) A levitated ferrimagnetic microsphere serves as an optomagnonic cavity. The microsphere exhibits uniaxial anisotropy and we assume that its magnetization is homogeneous, pointing initially along the direction of an external magnetic field. (b) The intracavity field couples via optomagnonic effects to the magnetization which in turn couples to the rotation through the magnetic anisotropy. (c) Schematic illustration of the relevant frequencies of the system and the pumping scheme. Two optical modes have frequencies ω_1 and ω_2 separated by the frequency of the magnon mode, i.e. $\omega_1 - \omega_2 = \omega_B$. One of the two modes is pumped in resonance with the laser frequency ω_L .

wavelength can drive simultaneously two internal optical modes of the levitated particle which satisfy the so-called *triple-resonance condition* where the frequency difference between the cavity modes equals the magnetization's precession frequency [69, 73]. In other words, transitions between the modes can occur through emission or absorption of a magnon. The triple-resonance condition can be fulfilled in the visible/near-infrared part of the electromagnetic spectrum, where the frequency splitting between neighboring Mie modes for micrometer-sized particles is in the range of a few GHz, the typical frequency of magnons [66]. We consider the only source of birefringence (and thus of torque) to be magnetic. This is valid for example for an Yttrium Iron Garnet (YIG) sphere. For magnetic dielectric particles which also exhibit op-

tical or geometric anisotropy [80–83], the model can be generalized accordingly. Our model takes optical losses and magnetic damping into consideration. The latter corresponds to damping of the magnetization precession, i.e., the relaxation to its equilibrium configuration [84]. For the coupling of the confined light to the particle magnetization we focus on the Faraday effect (circular birefringence), relegating consideration of the Cotton-Mouton effect (linear birefringence) to Sec. VIII A. The magnetization and the orientation of the particle are coupled by a magnetocrystalline anisotropy, such that a mechanical torque can be induced. We assume that the material exhibits uniaxial crystalline anisotropy, such that the magnetization, in the absence of a magnetic field, is aligned either parallel to the anisotropy axis, in the case of an easy-axis magnet, or perpendicular to it, in the case of a hard-axis magnet. We assume that the translational degrees of freedom are completely decoupled from the rest, namely, we neglect effects related to the center of mass motion of the particle. We therefore do not explicitly include the trapping potential in our model. We discuss briefly deviations from these assumptions in Sec. VIII.

A suitable material for an experimental realization of this system is YIG, since it exhibits ferrimagnetic properties at room temperature and shows high transparency in the near-infrared. Further, it has a large Faraday rotation per unit length $\theta_F = 240^\circ/\text{cm}$ with a dielectric index of $\varepsilon \approx 5$ [61, 85] at these frequencies, making it the material of choice in the state-of-the-art optomagnonic experiments [69–73]. In the following we investigate the proposed model for parameter values corresponding to YIG, although the framework applies in general for other materials too.

A. Hamiltonian

The Hamiltonian describing the system reads

$$\hat{H} = \hat{H}_{\text{Sp}} + \hat{H}_{\text{Cav}} + \hat{H}_{\text{OM}} \quad (1)$$

where \hat{H}_{Sp} is the Hamiltonian of the freely rotating magnetic sphere in the presence of the magnetic field and \hat{H}_{Cav} that of the optical modes confined in the dielectric sphere. \hat{H}_{OM} describes the coupling between the optical modes and the magnetization of the sphere. The operator character of the quantities is represented by the “hat” notation. In the following we present each term in detail.

The first term in Eq. (1) is given by

$$\hat{H}_{\text{Sp}} = \frac{\hbar^2 \hat{\mathbf{L}}^2}{2I} - \hbar\gamma \hat{\mathbf{S}} \cdot \mathbf{B}_0 - \hbar^2 D (\hat{\mathbf{S}} \cdot \mathbf{e}_3(\hat{\Omega}))^2, \quad (2)$$

where the first term is the kinetic energy of the rotational motion with dimensionless angular momentum $\hat{\mathbf{L}} = (\hat{L}_x, \hat{L}_y, \hat{L}_z)$ and $I = 2mR^2/5$ the moment of inertia

of a sphere of radius R and mass m . In the following we will express the inertia in terms of a rotation frequency of the rigid solid $\omega_I = \hbar/I$.

The second term in Eq. (2) corresponds to the Zeeman energy describing the interaction between the particle’s magnetization and the homogeneous magnetic field \mathbf{B}_0 . For the Kittel mode, all spins precess in phase and can be described by the dimensionless macrospin $\hat{\mathbf{S}} = (\hat{S}_x, \hat{S}_y, \hat{S}_z)$, which relates to the magnetization as $\hat{\mathbf{M}} = \hat{\mathbf{S}}M_S/S$ with $S = |\mathbf{S}|$ the total spin of the sample and M_S the saturation magnetization. $\gamma = 1.76 \cdot 10^{11} \text{ s}^{-1} \text{ T}^{-1}$ denotes the absolute value of the gyromagnetic ratio. We consider a magnetic field parallel to the z axis, namely $\mathbf{B}_0 = B_0 \mathbf{e}_z$, such that the Zeeman energy of the Hamiltonian reduces to $-\hbar\gamma \hat{S}_z B_0$ and we denote $\gamma B_0 = \omega_B$ as the Larmor precession frequency. For a sphere, this corresponds to the frequency of the Kittel mode. A magnon corresponding to this mode has energy $\hbar\omega_B$.

The third term in Eq. (2) accounts for uniaxial magnetocrystalline anisotropy (cubic anisotropy will be discussed in Sec. VIII B). The anisotropy axis is fixed to the particle and labeled as $\mathbf{e}_3(\hat{\Omega})$. As $\mathbf{e}_3(\hat{\Omega})$ depends on the Euler angles $\hat{\Omega}$, this term couples the spin with the orientation of the sphere with coupling constant $\omega_D = \hbar D$. Here $|D| = K_u V / (\hbar S)^2$ [86, 87] denotes the anisotropy strength with K_u the anisotropy energy density and V the volume of the particle. For $D > 0$, $\mathbf{e}_3(\hat{\Omega})$ is called an “easy axis”, i.e. the interaction energy is minimized if the magnetization and \mathbf{e}_3 are parallel. For $D < 0$, $\mathbf{e}_3(\hat{\Omega})$ is a “hard axis”, and in this case it is energetically favorable for the magnetization to lie in the plane perpendicular to \mathbf{e}_3 .

The orientation of $\mathbf{e}_3(\hat{\Omega})$ is defined by an operator specified by the Euler angles $\hat{\Omega} = \{\hat{\alpha}, \hat{\beta}, \hat{\gamma}\}$, such that $\mathbf{e}_3(\hat{\Omega})$ is given in terms of elements of the rotation matrix $R(\hat{\Omega})$ (Eq. (C1) and (C2)) connecting the fixed laboratory frame $O\mathbf{e}_x\mathbf{e}_y\mathbf{e}_z$ to the rotating frame $O\mathbf{e}_1\mathbf{e}_2\mathbf{e}_3$ (which we call the body frame): $(\mathbf{e}_1, \mathbf{e}_2, \mathbf{e}_3)^T = R(\hat{\Omega})(\mathbf{e}_x, \mathbf{e}_y, \mathbf{e}_z)^T$ (see Fig. 2). Note that from now on for simplicity we write \mathbf{e}_3 without the explicit dependence on $\hat{\Omega}$.

The cavity Hamiltonian \hat{H}_{Cav} describes the electromagnetic field inside the particle and is given by

$$\hat{H}_{\text{Cav}} = \frac{1}{2} \int d^3\mathbf{r} \left(\varepsilon_0 \hat{\mathbf{E}}^*(\mathbf{r}, t) \bar{\varepsilon} \hat{\mathbf{E}}(\mathbf{r}, t) + \frac{1}{\mu_0} \hat{\mathbf{B}}^2(\mathbf{r}, t) \right) \quad (3)$$

with ε_0 and μ_0 denoting, respectively, the vacuum permittivity and permeability, and $\bar{\varepsilon}$ the static part of the effective relative permittivity tensor that depends on the magnetization \mathbf{M} . Considering only the Faraday effect and a saturation magnetization along the z axis, the permittivity tensor is given by

$$\varepsilon(\mathbf{M}) = \bar{\varepsilon} + \delta\varepsilon, \quad (4)$$

with the static

$$\bar{\varepsilon} = \begin{pmatrix} \varepsilon & -ifM_z & 0 \\ ifM_z & \varepsilon & 0 \\ 0 & 0 & \varepsilon \end{pmatrix}, \quad (5)$$

and dynamical part

$$\delta\varepsilon = \begin{pmatrix} 0 & 0 & ifM_y \\ 0 & 0 & -ifM_x \\ -ifM_y & ifM_x & 0 \end{pmatrix}. \quad (6)$$

Here ε denotes the relative isotropic permittivity of the unmagnetized material, and f a material-dependent constant. It is related to the Faraday rotation per unit length θ_F ,

$$\theta_F = \frac{\omega f M_S}{2c\sqrt{\varepsilon}}, \quad (7)$$

for optical frequency ω and vacuum speed of light c . The decomposition into a static and dynamical part as given in Eqs. (4)-(6) is valid for small deviations of the magnetization with respect to the z -axis, such that M_z can be considered approximately constant $M_z \approx M_S$ ($M_{x,y}/M_S \ll 1$). The static magnetization causes a Zeeman-like splitting of the optical Mie modes [66], i.e. it lifts the $(2l+1)$ -degeneracy with respect to the azimuthal number $-l \leq m \leq l$, where l is the angular mode number. This splitting is in the GHz range [66].

The electric and magnetic intracavity field, $\hat{\mathbf{E}}$ and $\hat{\mathbf{B}}$, are quantized in the usual way such that \hat{H}_{Cav} is written in terms of the cavity operators \hat{a}_k and the corresponding frequencies ω_k (with k labelling the mode indices) as

$$\hat{H}_{\text{Cav}} = \sum_k \hbar\omega_k \left(\hat{a}_k^\dagger \hat{a}_k + \frac{1}{2} \right). \quad (8)$$

The optomagnonic Hamiltonian \hat{H}_{OM} is derived from the time-averaged electromagnetic energy [60, 62]

$$\bar{U} = \frac{1}{4}\varepsilon_0 \int d^3\mathbf{r} \sum_{ij} E_i^*(\mathbf{r}, t) \delta\varepsilon_{ij}(\mathbf{M}) E_j(\mathbf{r}, t). \quad (9)$$

We are interested in the interaction between the Kittel mode and a single pair of WGMs for which the optomagnonic interaction Hamiltonian, after quantizing the electric field $\mathbf{E}(\mathbf{r}, t) \rightarrow \hat{\mathbf{E}}^+(\mathbf{r}, t) = \sum_k \mathbf{E}_k(\mathbf{r}) \hat{a}_k(t)$ (with $\mathbf{E}_k(\mathbf{r})$ indicating the electric field of the k -th eigenmode), can be expressed as [69]

$$\hat{H}_{\text{OM}} = \hbar g (\hat{S}_+ \hat{a}_1^\dagger \hat{a}_2 + \hat{S}_- \hat{a}_2^\dagger \hat{a}_1), \quad (10)$$

where $\hat{S}_\pm = \hat{S}_x \pm i\hat{S}_y$. The optomagnonic coupling constant g is defined as

$$g = -\frac{\varepsilon_0 f M_S}{4\hbar S} \tilde{g} \quad (11)$$

Table I. Definition and values of the relevant frequencies and couplings in the system scaled by the total spin S . The values correspond to the physical parameters given in Table II and are given in terms of the magnon frequency $\omega_B \equiv \gamma B_0 = 10^{10} \text{ s}^{-1}$, corresponding to an applied magnetic field of ~ 60 mT. Note that the full dependence of the optomagnonic coupling g on R cannot be obtained analytically, due to the non-trivial dependence of the transition amplitude \tilde{g} on R (see Fig. 3).

Definition	Value (for R in μm)
$\omega_I S \equiv \hbar S / I = 5\hbar S / (2mR^2)$	$2.15 \cdot 10^{-8} \omega_B / R^2$
$\omega_D S \equiv \hbar D S = K_u V / (\hbar S)$	$2.32 \cdot 10^{-1} \omega_B$
$g S = \frac{\varepsilon_0 f M_S}{4\hbar} \tilde{g}$	$5.596 \cdot 10^{-2} \omega_B / R$

Table II. Values of the physical parameters used in the calculations. The values correspond to YIG [61, 89], however, the framework holds generally. Note that we choose $m_i = 0$ such that the coupling strength is maximized (see Appendix B).

Parameter and values	Description
$\rho_m = 5 \cdot 10^3 \text{ kg m}^{-3}$	Mass density
$S = \rho_m / 738 \text{ amu}$	Total spin
$K_u = 10^3 \text{ J/m}^3$ ^a	Magnetic anisotropy constant
$\varepsilon = 5$	Relative permittivity
$n = 2.2$	Refractive index
$\theta_F = 240^\circ / \text{cm}$	Faraday rotation
$M_S = 140 \text{ kA/m}$	Saturation magnetization
$\lambda_0 = 1500 \mu\text{m}$	Laser wavelength
$m_i = 0$	Initial azimuthal mode number
$\eta_G = 10^{-4}$	Gilbert damping parameter

^a For the cubic symmetry of YIG one finds two constants for the anisotropy density in the literature. Here we approximate the uniaxial constant with a value in the order of the first-order cubic anisotropy constant. See Sec. VIII B for details.

with \tilde{g} (given in Appendix B) denoting the transition amplitude between two Zeeman-split Mie modes. Here the selection rule for the initial and final azimuthal mode numbers $m_f - m_i = 1$ is fulfilled, and we assume that the frequency splitting between two neighboring modes satisfies the triple-resonance condition. The triple resonance can be achieved by tuning the frequency of the Kittel mode by the external magnetic field \mathbf{B}_0 . For a micron sized YIG sphere $g \sim 0.03 \text{ Hz}$. This coupling is enhanced by driving one of the two optical modes, by a factor given by the square root of the number of circulating photons in the cavity [68, 88].

The optical modes are driven externally by a laser, described by adding a driving term $i\hbar\epsilon_{L1,2} \left(\hat{a}_{1,2}^\dagger e^{-i\omega_{\text{Las}} t} - \hat{a}_{1,2} e^{i\omega_{\text{Las}} t} \right)$ to the Hamiltonian. The parameter $\epsilon_{Li} = \sqrt{\frac{\kappa_{\text{rad}} P_i}{\hbar\omega_{\text{Las}}}}$ depends on the laser power P_i and the radiative decay rate κ_{rad} (see

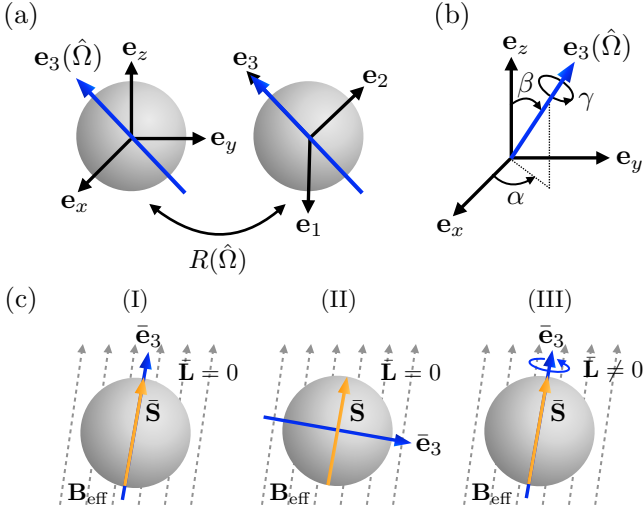


Figure 2. Definition of the Euler angles. (a) The rotation matrix $R(\hat{\Omega})$ aligns the fixed laboratory frame $O\mathbf{e}_x\mathbf{e}_y\mathbf{e}_z$ with the body frame $O\mathbf{e}_1\mathbf{e}_2\mathbf{e}_3$ where $\mathbf{e}_3(\hat{\Omega})$ denotes the anisotropy direction. (b) The Euler angles correspond to three successive rotations that are necessary for aligning the lab frame with the frame in which \mathbf{e}_3 is fixed. (c) Steady state configurations of the system.

Eq. (A7)). Collecting all terms and working in a frame rotating with the laser frequency ω_{Las} , the total system Hamiltonian reads

$$\begin{aligned} \hat{H} = & \frac{1}{2}\hbar\omega_I\hat{\mathbf{L}}^2 - \hbar\omega_B\hat{S}_z - \hbar\Delta_1\hat{a}_1^\dagger\hat{a}_1 - \hbar\Delta_2\hat{a}_2^\dagger\hat{a}_2 \\ & - \hbar\omega_D(\hat{\mathbf{S}}\cdot\hat{\mathbf{e}}_3)^2 + \hbar g(\hat{S}_+\hat{a}_1^\dagger\hat{a}_2 + \hat{S}_-\hat{a}_2^\dagger\hat{a}_1) \\ & + i\hbar\epsilon_{L1}(\hat{a}_1^\dagger - \hat{a}_1) + i\hbar\epsilon_{L2}(\hat{a}_2^\dagger - \hat{a}_2) \end{aligned} \quad (12)$$

with detuning $\Delta_i = \omega_{\text{Las}} - \omega_i$. The assumption that the drive laser couples to both modes is a simplification that can be refined [90].

In Table I we summarize the relevant frequencies and couplings and show their dependence on the size of the particle in Fig. 3(a). The optomagnonic coupling g and the anisotropy strength ω_D have a similar magnitude while the inertia frequency ω_I is orders of magnitude smaller and decreases faster with particle radius. All the relevant values for the physical parameters appearing in the system are listed in Table II.

III. EQUATIONS OF MOTION

From the Hamiltonian in Eq. (12) we obtain the equations of motion for the set of operators $\hat{\xi} =$

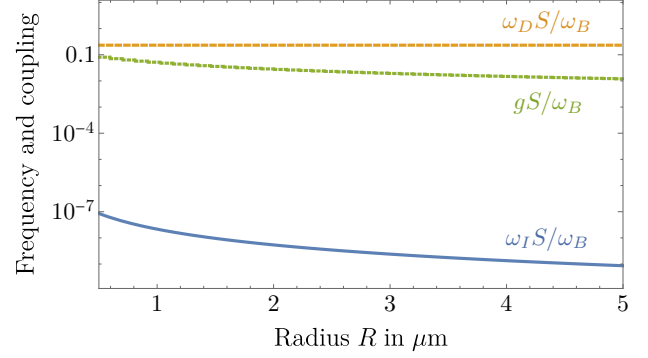


Figure 3. Frequencies and couplings defined in Table I as a function of the radius R . The values are given in units of the Larmor frequency $\omega_B = \gamma B_0$ which is controlled by the applied magnetic field and is typically in the GHz range. Note that the vertical axis is in logarithmic scale.

($\hat{\mathbf{e}}_3, \hat{\mathbf{L}}, \hat{\mathbf{S}}, \hat{a}_1, \hat{a}_1^\dagger, \hat{a}_2, \hat{a}_2^\dagger$) via the Heisenberg equation

$$\frac{d}{dt}\hat{\xi} = \frac{i}{\hbar}[\hat{H}, \hat{\xi}], \quad (13)$$

and focus on the classical limit by taking the average value of the operators over coherent states and disregarding any correlations and noise [91] (see Appendix C). In the following we denote $\langle \hat{\xi} \rangle = \xi$. We also add dissipative terms, which we discuss in detail below. The coupled equations of motion read

$$\begin{aligned} \dot{\mathbf{e}}_3 &= -\omega_I\mathbf{e}_3 \times \mathbf{L}, \\ \dot{\mathbf{L}} &= 2\omega_D(\mathbf{e}_3 \cdot \mathbf{S})(\mathbf{e}_3 \times \mathbf{S}) - \boldsymbol{\tau}_G, \\ \dot{\mathbf{S}} &= \mathbf{B}_{\text{eff}} \times \mathbf{S} - 2\omega_D(\mathbf{e}_3 \cdot \mathbf{S})(\mathbf{e}_3 \times \mathbf{S}) + \boldsymbol{\tau}_G, \\ \dot{a}_1 &= i\Delta_1 a_1 - igS_+ a_2 + \epsilon_{L1} - \frac{1}{2}\kappa a_1, \\ \dot{a}_2 &= i\Delta_2 a_2 - igS_- a_1 + \epsilon_{L2} - \frac{1}{2}\kappa a_2, \end{aligned} \quad (14)$$

where $\mathbf{B}_{\text{eff}} = -\omega_B\mathbf{e}_z + g(a_1^\dagger a_2 + a_2^\dagger a_1)\mathbf{e}_x + ig(a_1^\dagger a_2 - a_2^\dagger a_1)\mathbf{e}_y$. The evolution of the total angular momentum $\mathbf{J} = \mathbf{L} + \mathbf{S}$ is given by

$$\dot{\mathbf{J}} = \mathbf{B}_{\text{eff}} \times \mathbf{S}, \quad (15)$$

and the dynamics is given either in terms of (\mathbf{S}, \mathbf{L}) or (\mathbf{S}, \mathbf{J}) .

The equations of motion include cavity damping terms κ , which we consider to include only radiative losses [92], i.e. $\kappa = \kappa_{\text{rad}}$, although other sources, such as surface roughness, can also be relevant depending on the size of the particle. Furthermore, we introduced Gilbert damping to account for intrinsic damping of the spin by adding the torque $\boldsymbol{\tau}_G$ [84, 93],

$$\boldsymbol{\tau}_G = \frac{\eta_G}{S}\dot{\mathbf{S}} \times \mathbf{S} - \frac{\eta_G}{S}\omega_I\mathbf{S} \times (\mathbf{S} \times \mathbf{L}), \quad (16)$$

where η_G is a dimensionless damping parameter (in the order of 10^{-4} for YIG). The second term stems from the fact that the Gilbert damping is defined in the rotating (body) frame, describing the relative motion of the magnetization with respect to the lattice. Thus a coordinate transformation is required to include damping in the laboratory frame. This additional term gives rise to the Barnett effect, i.e. magnetization dynamics induced by rotation [44, 93]. Since Gilbert damping is solely due to internal forces, we subtracted $\boldsymbol{\tau}_G$ in the equation for $\dot{\mathbf{L}}$, such that the total angular momentum is only affected by the external torque (see Eq. (15)) [94]. This approximation neglects, for example, heating effects or damping into other magnon modes.

The dynamics described by Eq. (14) conserves two quantities:

$$\begin{aligned} |\mathbf{e}_3| &= \sqrt{R_{31}^2 + R_{32}^2 + R_{33}^2} = 1, \\ |\mathbf{S}| &= \sqrt{S_x^2 + S_y^2 + S_z^2} = S. \end{aligned} \quad (17)$$

Furthermore, for negligible Gilbert damping (i.e. $\eta_G/S \rightarrow 0$) [95], the equations of motion yield a third conserved quantity

$$\mathbf{e}_3 \cdot \mathbf{L} = \text{const.} \quad (18)$$

This is obtained from the first two equations of motion for $\boldsymbol{\tau}_G = \mathbf{0}$ as it imposes that $\dot{\mathbf{e}}_3 \cdot \mathbf{L} + \dot{\mathbf{L}} \cdot \mathbf{e}_3 = \frac{d}{dt}(\mathbf{e}_3 \cdot \mathbf{L}) = 0$. In this case, if $\mathbf{L}(t=0) = \mathbf{0}$, at any instant of time $\mathbf{e}_3(t) \cdot \mathbf{L}(t) = 0$, and thus, the sphere does not rotate around its anisotropy axis. The only possible angular motions are precession and libration, with angular speeds given by the components of \mathbf{L} perpendicular to \mathbf{e}_3 .

The equation of motion for \mathbf{L} can be recast in a more familiar form

$$\hbar \dot{\mathbf{L}} = \boldsymbol{\tau} = \hbar \mathbf{e}_3 \times 2\omega_D (\mathbf{e}_3 \cdot \mathbf{S}) \mathbf{S} = R \mathbf{e}_3 \times \mathbf{F}. \quad (19)$$

The angular torque $\boldsymbol{\tau}$ is therefore generated by the force $\mathbf{F} = \frac{2\hbar\omega_D}{R} (\mathbf{e}_3 \cdot \mathbf{S}) \mathbf{S}$. The torque $\boldsymbol{\tau}$ can be driven by a laser, which induces, via optomagnonic coupling, the spin dynamics. In particular, if the system's initial configuration is the undriven equilibrium point $\mathbf{S} \parallel \mathbf{e}_3 = \mathbf{e}_z$, the only source of initial motion is the laser drive. Any subsequent time evolution of the spin, and consequently any angular motion of the sphere, is generated by a combination of the optically induced torque and the torque by the external magnetic field. The latter is responsible for a Larmor precession of the spin around the direction of the magnetic field.

From the equations of motion Eq. (14) it can be further seen that in the absence of crystalline anisotropy, namely $\omega_D = 0$, the angular motion is completely decoupled from the optomagnonic part for $\eta_G = 0$, i.e. in this case one

recovers the dynamics for a pure optomagnonic system as treated for one optical mode in Ref. [62]. If Gilbert damping is considered $\eta_G \neq 0$, then there is a coupling of the angular motion to the spin due to conservation of angular momentum.

We will now proceed to characterize the dynamics of this driven dissipative system. We will first obtain the possible steady state configurations given by Eq. (14), and then study the light-spin-rotation dynamics for small perturbations around such steady states.

IV. STEADY STATE

We find the possible steady states of the system by setting $\frac{d\xi}{dt} = 0 \forall \xi$ in Eq. (14). Denoting by $\bar{\xi}$ the steady state value of the quantity $\xi(t)$, we find the following possible steady states, as depicted in Fig. 2(c):

$$\begin{aligned} \text{(I)} \quad & \bar{\mathbf{L}} = \mathbf{0}, \bar{\mathbf{e}}_3 \parallel \pm \bar{\mathbf{S}} \\ \text{(II)} \quad & \bar{\mathbf{L}} = \mathbf{0}, \bar{\mathbf{e}}_3 \perp \bar{\mathbf{S}} \\ \text{(III)} \quad & \bar{\mathbf{L}} \neq \mathbf{0}, \bar{\mathbf{e}}_3 \parallel \pm \bar{\mathbf{L}} \parallel \pm \bar{\mathbf{S}} \end{aligned} \quad (20)$$

with $\bar{\mathbf{S}} \parallel \pm \bar{\mathbf{B}}_{\text{eff}}$. In the case of a non-rotating sphere ($\bar{\mathbf{L}} = \mathbf{0}$), (I) minimizes the angular-spin interaction energy for an easy-axis anisotropy, whereas (II) minimizes the interaction energy for a hard-axis anisotropy. If $\bar{\mathbf{L}} \neq \mathbf{0}$, then the sphere rotates around \mathbf{e}_3 and $\bar{\mathbf{L}}$ must be parallel to $\bar{\mathbf{S}}$, which implies that $\bar{\mathbf{e}}_3 \parallel \pm \bar{\mathbf{S}}$.

For the steady states of the spin and the optical fields, we find a solution with a finite average number of circulating photons in both modes ($|\bar{a}_i|^2 \neq 0$) when both modes are simultaneously driven, $\epsilon_{Li} \neq 0$ (Supplement 1, Sec. 4). The light creates a deflection of the magnetization, such that in the steady-state

$$\begin{aligned} \bar{S}_x &= S \cos \phi \sin \theta, \\ \bar{S}_y &= S \sin \phi \sin \theta, \\ \bar{S}_z &= S \cos \theta. \end{aligned} \quad (21)$$

with the azimuthal angle ϕ

$$\phi = \arctan \left(\frac{\bar{a}_2^* \bar{a}_1 - \bar{a}_1^* \bar{a}_2}{\bar{a}_2^* \bar{a}_1 + \bar{a}_1^* \bar{a}_2} \right), \quad (22)$$

and the deflection θ from the z -axis

$$\theta = \arctan \left(\frac{2g}{\omega_B} |\bar{a}_1| |\bar{a}_2| \right), \quad (23)$$

which depends on the square root of the circulating photon number in each optical mode.

In the limit that the optically induced magnetic field is smaller than the external magnetic field, i.e. $\omega_B \gg$

$4g|\bar{a}_1||\bar{a}_2|$, the optical steady state reduces to

$$\bar{a}_1 = -\frac{\epsilon_{L1}}{i\left(\Delta_1 + \frac{2g^2|\bar{a}_2|^2S}{\omega_B}\right) - \frac{1}{2}\kappa}, \quad (24)$$

where \bar{a}_2 is given by

$$i\Delta_2\bar{a}_2 + i\frac{2g^2S}{\omega_B}\frac{\epsilon_{L1}^2}{\left(\Delta_1 + \frac{2g^2|\bar{a}_2|^2S}{\omega_B}\right)^2 + \frac{1}{4}\kappa^2}\bar{a}_2 - \frac{1}{2}\kappa\bar{a}_2 + \epsilon_{L2} = 0. \quad (25)$$

Note that it is equivalent to first express \bar{a}_2 as a function of \bar{a}_1 and then solve the corresponding equation for \bar{a}_1 . By driving only one optical mode, the steady state of the undriven mode equals zero. As a consequence, the steady state value of the spin is unaffected by the light, as can be seen from Eqs. (22) and (23), and the effect of the driving is purely dynamical. In the following we focus on a pumping scheme where both modes are driven (Fig. 1(c)).

For the range of laser powers considered (up to 1 W) the deflection angle scales linearly with the power and we obtain $\theta \approx 0.2\sqrt{P_1P_2}^\circ/W$ for a sphere of size $R = 1 \mu\text{m}$ (taking $\Delta_1 = -\omega_B$, $\Delta_2 = 0$). Such small deflection angle justifies the static Mie splitting determined by M_S along the z -axis (see Sec. II) also in the presence of light.

The steady states given in Eq. (20) are not necessarily stable. In particular for \mathbf{e}_3 an easy-axis (hard-axis), the perpendicular (parallel) steady state configuration is always unstable. Further, we observe in the following that the dynamics do not fully converge to the steady states in the considered timescales due to the low dissipation in the system.

V. DYNAMICS

Having characterized the steady states of the system we now turn to study numerically the dynamics of the system under an optical drive. For concreteness we consider an easy-axis magnet, i.e. $D > 0$, and an initial state in which the spin and the anisotropy axis are aligned parallel along the external magnetic field, namely $\mathbf{e}_3(0) = \mathbf{S}(0)/S = \mathbf{e}_z$. For a hard-axis magnet we would retrieve the same results by choosing an initial configuration in which the anisotropy axis is perpendicular to the spin and therefore do not explicitly discuss them. For the optical fields we assume that the initial conditions are given by Eqs. (24) and (25). We consider driving laser powers such that the deviation of the steady state with respect to the chosen initial configuration is sufficiently small. Thus, we expect the system to oscillate around this configuration with an amplitude that depends on the driving power. Since we consider a Mie splitting given by the static magnetization

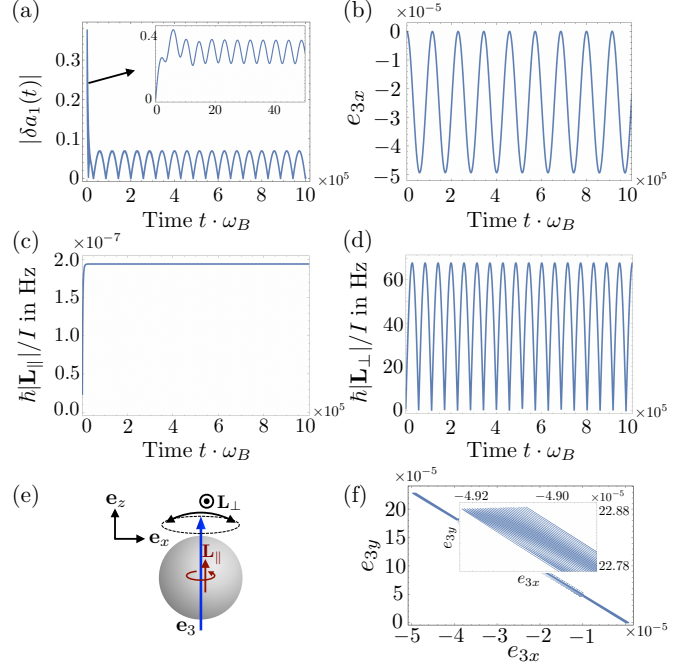


Figure 4. Dynamics of a sphere of size $R = 1.5 \mu\text{m}$ with initial configuration $\mathbf{S} \parallel \mathbf{e}_3 \parallel \mathbf{e}_z$ and $\mathbf{L} = \mathbf{0}$. The system is red detuned with $P_2 = 0.02 \text{ W}$ and $P_1 = P_2/2$. (a) Amplitude fluctuation of the cavity mode 1. The inset shows the initial time evolution of the system. After a transient period, the cavity dynamics is modulated by (b) the dynamics of the anisotropy axis \mathbf{e}_3 . Angular momentum (c) parallel \mathbf{L}_\parallel and (d) perpendicular \mathbf{L}_\perp to \mathbf{e}_3 . As schematically depicted in (e), \mathbf{L}_\parallel gives the angular speed of rotation of the sphere around the anisotropy axis via $\hbar|\mathbf{L}_\parallel|/I$ and \mathbf{L}_\perp is related to the libration and precession of \mathbf{e}_3 , shown in the xy plane (f). The time is given in terms of the magnon frequency $\omega_B = 10^{10} \text{ s}^{-1}$.

along the z -axis, our model requires modifications for initial configurations where the spin is not approximately along the z direction, and it breaks down for pumping powers that exceed a critical value such that the z component of the spin deviates too far from the z -axis. In this case the so-called Suhl instabilities can further occur, opening new dissipation channels [96].

We consider two pumping schemes depicted in Fig. 1(c): First, the optical cavity-mode with higher frequency is pumped in resonance, such that $\Delta_1 = 0$ and $\Delta_2 = \omega_B$, which we refer to as blue detuning and describes magnon emission; second, the mode with lower frequency is pumped in resonance, such that $\Delta_1 = -\omega_B$ and $\Delta_2 = 0$, which is related to a magnon absorption and which we call red detuning. These processes can be interpreted as cavity-enhanced Stokes and anti-Stokes Brillouin scattering. The Gilbert damping included in the equations of motion Eq. (14) renders the north pole a stable equilibrium point in the absence of driving. With

driving, for the red detuning scheme, the north pole is stable whereas the south pole results in runaway solutions which can lead to limit cycles or chaotic dynamics. For blue detuning, the south pole can become a stable point depending on the driving power and on the detuning. For a more detailed discussion see Ref. [62]. Note that we choose $P_1 = P_2/2$ for our simulations. This is not a restrictive assumption and changing the ratio between P_1 and P_2 does not change the results qualitatively.

We show the time evolution of $|\delta a_1(t)| = |\bar{a}_1 - a_1(t)|$, i.e. the deviations of the amplitude of the higher frequency optical mode from its steady state value, and of \mathbf{e}_3 in Figs. 4(a) and (b) for the red detuned pumping scheme. The initial configuration is such that the particle has no initial rotational motion, i.e. $\mathbf{L}(t=0) = \mathbf{0}$. We shortly discuss the dynamics of an initially rotating particle, $\mathbf{L}(t=0) \neq \mathbf{0}$, in Appendix E. This latter case is especially relevant if one starts with an unmagnetized particle at rest and then magnetizes it, which induces an initial rotation due to the Einstein-de Haas effect [43].

The cavity field dynamics are modulated by the angular motion and, at short times, the dominant contributions are due to the optomagnonic coupling and the fast spin dynamics. To gain further insight into the driven angular motion, we show in Fig. 4(c) the dynamics of the absolute value of the components of \mathbf{L} parallel and perpendicular to \mathbf{e}_3 . The parallel component of the angular momentum \mathbf{L}_{\parallel} gives the angular speed of rotation of the sphere around its magnetic anisotropy axis via $\hbar|\mathbf{L}_{\parallel}|/I$ in the lab frame, while the perpendicular component \mathbf{L}_{\perp} is related to libration and precession of \mathbf{e}_3 . We notice that $|\mathbf{L}_{\parallel}|$ quickly increases but then stays stationary. This is due to the quick spin dynamics during the initial evolution from the starting configuration to close-to-steady-state oscillation. After the transient dynamics the effects of spin damping, as described by the Gilbert damping term, become negligible and $|\mathbf{L}_{\parallel}|$ is conserved.

VI. POWER SPECTRUM ANALYSIS

As we observed in the previous section, the dynamics of the cavity optical modes exhibit a transitory behavior followed by an evolution modulated by the anisotropy axis dynamics. Namely, at short times the deviations $|\delta a_i(t)|$ oscillate with the same frequency as the spin oscillates and then adapts to the oscillations of the magnetic anisotropy axis. The frequencies associated with each of these dynamics are imprinted in the power spectrum of the light, as we show now.

First, we write the cavity fields as

$$a_i(t) = \bar{a}_i + \delta a_i(t), \quad (26)$$

such that $\delta a_i(t)$ represents the deviation of a_i from its steady state value \bar{a}_i . We then consider the Fourier trans-

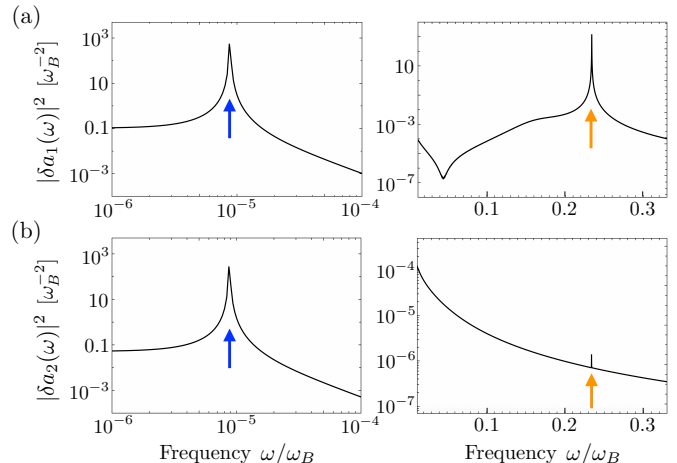


Figure 5. Logarithmic power spectrum of the cavity optical modes (a) δa_1 and (b) δa_2 for a red detuned system with $P_2 = 0.02$ W and $P_1 = P_2/2$. The sphere has a radius of $R = 1.5 \mu\text{m}$, the initial state is $\mathbf{S} \parallel \mathbf{e}_3 \parallel \mathbf{e}_z$, and $\mathbf{L} = \mathbf{0}$, corresponding to the results presented in Fig. 4(a). Both modes yield a peak in the spectrum at a frequency of ~ 90 kHz (highlighted by the blue arrow) which corresponds to the induced angular motion. At a frequency of ~ 2.33 GHz a second peak can be observed which corresponds to the fast oscillations at small times (orange arrow), related to the magnetization's transient dynamics. Note that the horizontal axis in the right panel is in linear scale. The frequency is given in terms of the magnon frequency $\omega_B = 10^{10} \text{ s}^{-1}$.

form of $\delta a_i(t)$

$$\mathcal{F}[\delta a_i(t)] = \int_0^{+\infty} \delta a_i(t) e^{i\omega t} dt = \delta a_i(\omega), \quad (27)$$

from which we compute the power spectrum $|\delta a_i(\omega)|^2$.

We show in Fig. 5 the absolute value of the fluctuations and the resulting spectrum for an initially non-rotating sphere ($R = 1.5 \mu\text{m}$) under a red detuned drive. The spectra for both modes show a clear peak at a frequency of ~ 90 kHz. This peak corresponds to the oscillation frequency of the cavity field amplitude after the initial transitory behavior. In fact, this frequency is the same as the oscillation frequency of the magnetic anisotropy axis and is a fingerprint of the modulation of the cavity dynamics by the sphere's angular motion. Further, the spectra yield a second peak at a frequency ~ 2.33 GHz, that is related to optomagnonic induced transient spin oscillations including the effects of its coupling to the angular motion (a frequency shift). The finite linewidth of the Lorentzian shaped peaks is governed by the low dissipation and the finite simulation time. The dip around 0.4 GHz in the power spectrum of mode 1 can be attributed to a Fano resonance [97] emerging from the coupling between spin and angular momentum which, close to the steady state, act like two coupled harmonic oscillators. Such Fano res-

onances have also been observed in optomechanical systems [98, 99].

To better understand the origin of the observed resonance frequencies, we consider now the linearized version of the equations of motion Eq. (14) and derive the susceptibility of the cavity-field fluctuations. For that, we consider small displacements from the steady state

$$\xi(t) = \bar{\xi} + \delta\xi(t),$$

and retain in the equations of motion only linear terms in the fluctuations. Since the considered optomagnonic effects are weak, to a first approximation we assume that the steady state of the spin and the anisotropy axis is sufficiently close to the north pole, i.e. $\bar{S}_{x,y}/S = \bar{e}_{3x,y} \approx 0$ and $\bar{S}_z/S = \bar{e}_{3z} \approx 1$, and take a non-rotating sphere, $\bar{\mathbf{L}} = \mathbf{0}$. Relegating the detailed calculations to the Appendix F, we obtain the following susceptibility for the fluctuations δa_1 in frequency space:

$$\chi_1(\omega) = \left[-i(\omega + \Delta_1 - 2g^2 S |\bar{a}_2|^2 \chi_+(\omega)) + \frac{\kappa}{2} \right]^{-1}, \quad (28)$$

where

$$\begin{aligned} \chi_+^{-1}(\omega) &= \omega - \tilde{\omega}_B - \frac{|\bar{B}_+|^2}{2\omega} + \frac{4\omega_D^2 \omega_I S^3}{2\omega_D \omega_I S^2 - \omega^2} \\ &\quad + \frac{2g^2 S |\bar{a}_1|^2 (\omega - \Delta_2 - i\kappa/2)}{\kappa^2/4 + (\omega - \Delta_2)^2} - \frac{\bar{B}_+^2 \bar{B}_+^{*2}}{4\omega^2} \chi_-(\omega), \\ \chi_-^{-1}(\omega) &= \omega + \tilde{\omega}_B - \frac{|\bar{B}_+|^2}{2\omega} - \frac{4\omega_D^2 \omega_I S^3}{2\omega_D \omega_I S^2 - \omega^2} \\ &\quad + \frac{2g^2 S |\bar{a}_1|^2 (\omega + \Delta_2 - i\kappa/2)}{\kappa^2/4 + (\omega + \Delta_2)^2} \\ &\quad - \frac{2g^2 S |\bar{a}_2|^2 (\omega - \Delta_1 - i\kappa/2)}{\kappa^2/4 + (\omega - \Delta_1)^2}, \end{aligned}$$

with $\tilde{\omega}_B = \omega_B + 2\omega_D S$ and $\bar{B}_+ = 2g\bar{a}_1\bar{a}_2^*$. The peaks of the power spectrum are obtained by the poles of the imaginary part of $\chi_1[\omega]$, and are approximately given by the equation

$$(\omega + \Delta_1) \left(\omega - \tilde{\omega}_B - \frac{|\bar{B}_+|^2}{2\omega} + \frac{4\omega_D^2 \omega_I S^3}{2\omega_D \omega_I S^2 - \omega^2} \right) - 2Sg^2 |\bar{a}_2|^2 = 0. \quad (29)$$

For the values used in Fig. 5, we obtain from Eq. (29) two resonance frequencies: $\omega_L/(2\pi) \approx 88.7$ kHz and $\omega_H/(2\pi) \approx 2.33$ GHz, in agreement with the numerical results shown in Fig. 5.

The high-frequency peak ω_H can be obtained by discarding the terms $\frac{4\omega_D^2 \omega_I S^3}{2\omega_D \omega_I S^2 - \omega^2}$ and $|\bar{B}_+|^2/(2\omega)$ in Eq. (29). This corresponds to neglecting the dynamics of \mathbf{e}_3 (a good approximation for describing the dynamics of the system for periods $\ll 1/\omega_I$), and to considering the

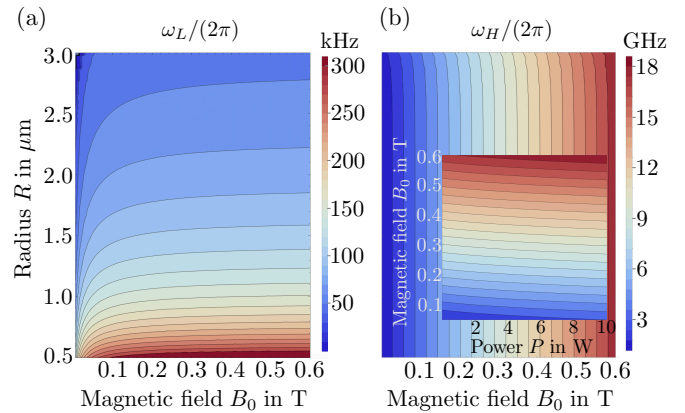


Figure 6. Phase diagrams for a red detuned system. Values of the (a) low ω_L and (b) high ω_H resonance frequency depending on the radius R and the magnetic field B_0 for $P_2 = 0.02$ W and $P_1 = P_2/2$. The inset shows the dependence on B_0 and the laser power P_2 for an increased optomagnonic coupling $g' = 10g$ and $R = 1.5 \mu\text{m}$. The resonance frequencies are obtained from the imaginary part of the eigenvalues of the linearized system Eq. (F1).

optically induced magnetic field negligible compared to the applied external magnetic field. Under these approximations, the high-frequency peak is given by $\omega_H \approx \tilde{\omega}_B$. The coupling between spin and angular motion changes the spin precession frequency by a factor $2\omega_D S$ compared to the uncoupled case [100]. Note that this approximation for the shift in the spin precession frequency is volume independent and only depends on the material properties like the anisotropy constant or the density. This can also be seen in Fig. 6 (for radii up to $R \approx 2.5 \mu\text{m}$) where we show the dependence of the resonance frequencies on the particle radius and the external magnetic field. Regarding its dependence on the laser power, we observe that in principle ω_H is shifted to higher frequencies for larger powers. However, for the considered values of the optomagnonic coupling, this effect is negligible. Nonetheless, the dependence is shown in the inset of Fig. 6(b) for an increased coupling $g' = 10g$. In this case we further find that an additional peak close to the lower frequency peak appears in the spectrum for power values $P_2 > 0.1$ W. The same can be observed for the unchanged optomagnonic coupling strength for smaller magnon frequencies. However, this peak is weak in amplitude and thus we do not further investigate it.

An initial rotation does not change the power spectrum qualitatively but decreases the frequency of the lower peak ω_L . Such effects are typically small for $L \sim S$, which corresponds to frequencies of $\sim 100/(2\pi)$ Hz. For $L \gg S$, rotations yield a more pronounced frequency shift, for instance, for $L = 10^3 S$ ($L = 10^4 S$) the position of the lower peak is at ~ 80 kHz (~ 40 kHz). For large L gyroscopic effects become more dominant such

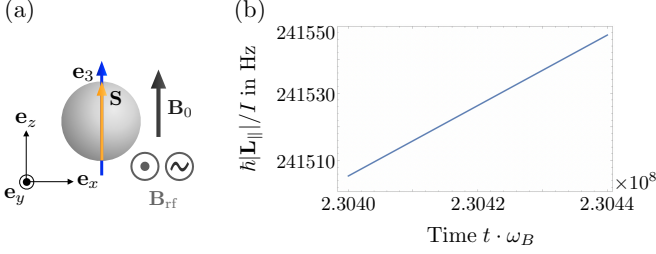


Figure 7. (a) Illustration of the driven system. An oscillating magnetic field is applied perpendicular to the bias field B_0 . (b) Angular speed of rotation of the sphere around the anisotropy axis. The system is red detuned with $R = 1.5 \mu\text{m}$, $P_2 = 0.02 \text{ W}$ and $P_1 = P_2/2$ and initial configuration $\mathbf{S} \parallel \mathbf{e}_z \parallel \mathbf{e}_z$ and $\mathbf{L} = \mathbf{0}$. The amplitude of the driving magnetic field is given by $a_{\text{rf}} = 0.01$. The angular speed reached after $\sim 20 \text{ ms}$ is 12 orders of magnitude higher than the corresponding rotation of the undriven system shown in Fig. 4(c). The time is given in terms of the magnon frequency $\omega_B = 10^{10} \text{ s}^{-1}$.

that the torque due to the fast angular rotation stabilizes the anisotropy axis and thus decreases its oscillation frequency. As mentioned before, the discussion presented here is valid as long as the initial state of the system is close to its steady state.

VII. RF DRIVEN SYSTEM

To enhance the peak in the power spectrum related to the spin oscillations as well as the angular speed of rotation of the sphere, we take inspiration from ferromagnetic resonance experiments where a periodic magnetic field is applied perpendicular to the bias field, as schematically depicted in Fig. 7(a). A resonant drive corresponds to an oscillating driving field with frequency matching the magnetization's precession frequency. We thus include in our model a periodic magnetic field $\mathbf{B}_{\text{rf}} = a_{\text{rf}} B_0 \cos(\omega_{\text{rf}} t) \mathbf{e}_y$ where a_{rf} is a dimensionless factor describing the ratio between the FMR drive amplitude and the bias field strength (given by B). The Hamiltonian Eq. (12) is then augmented by the term

$$\hat{H}_{\text{rf}} = -\hbar a_{\text{rf}} \omega_B \hat{S}_y \cos(\omega_{\text{rf}} t). \quad (30)$$

The amplitude of the driving field can be related to the excitation power P_{mw} by $a_{\text{rf}} \omega_{\text{rf}} = 2\sqrt{\kappa_{\text{mw}} P_{\text{mw}} / (\hbar \omega_{\text{mw}})}$ with the microwave frequency ω_{mw} and coupling to the antenna κ_{mw} . The value of the latter can be kept close to the intrinsic magnon dissipation $\kappa_m \sim 1 \text{ MHz}$ [74, 101] to enable a maximal power flow into the magnet. Thus, for $\omega_{\text{mw}} / (2\pi) = 10 \text{ GHz}$ this corresponds to $P_{\text{mw}} \sim a_{\text{rf}}^2 \text{ pW}$ which is comparable to excitation powers used in Ref. [102].

This external drive not only enhances the visibility of the peaks in the cavity spectrum but also introduces

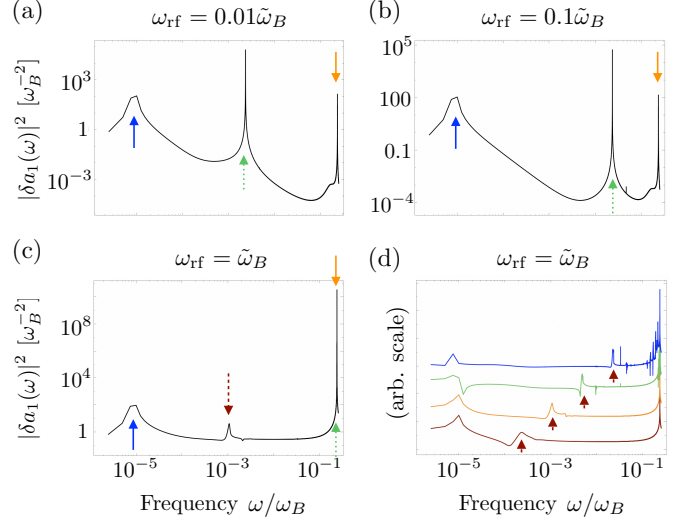


Figure 8. Logarithmic power spectrum of the driven system of δa_1 for $a_{\text{rf}} = 10^{-3}$ and FMR frequency (a) $\omega_{\text{rf}} = 0.01\tilde{\omega}_B$, (b) $\omega_{\text{rf}} = 0.1\tilde{\omega}_B$, (c) $\omega_{\text{rf}} = \tilde{\omega}_B$. The system is red detuned with $P_2 = 0.02 \text{ W}$, $P_1 = P_2/2$ and $R = 1.5 \mu\text{m}$. The initial state is $\mathbf{S} \parallel \mathbf{e}_3 \parallel \mathbf{e}_z$, and $\mathbf{L} = \mathbf{0}$. The FMR frequency is imprinted in the spectrum by a corresponding peak (marked by the green, dotted arrow). For $\omega_{\text{rf}} = \tilde{\omega}_B$, additionally to the peaks at $\sim 100 \text{ kHz}$ and $\sim 2.33 \text{ GHz}$, the power spectrum yields a third peak (red, dashed arrow) that depends on the amplitude of the driving field (d). The driving field amplitude values are $a_{\text{rf}} = 10^{-4}, 10^{-3}, 10^{-2}, 10^{-1}$ from bottom to top. The frequency is given in terms of the magnon frequency $\omega_B = 10^{10} \text{ s}^{-1}$.

new features depending on the frequency of the drive. Fig. 8(a)-(c) shows the power spectrum of cavity mode 1 for different FMR frequencies ω_{rf} which are visible by a corresponding peak. If we choose the FMR frequency ω_{rf} to match the shifted spin precession frequency $\omega_H \approx \tilde{\omega}_B$, the additional field enhances the amplitude of the higher frequency peak ω_H and yields a third peak with intermediate frequency between ω_L and ω_H . This extra resonance made visible by the rf driving field is due to a mismatch between the optical modes frequency difference and the shifted magnetization precession frequency due to the coupling to angular motion. This is a consequence of the nonlinearity of the system and is not captured by the analytically calculated susceptibilities, so we have to resort to numerical analysis. The position of the appearing peak depends on the driving field amplitude (Fig. 8(d)), namely, for larger amplitudes this peak shifts to higher frequencies.

The driving magnetic field also affects the angular motion of the particle. In fact, it increases the angular speed of rotation of the sphere around the anisotropy axis. This can be seen in Fig. 7(b) where we show $\hbar|\mathbf{L}_{\parallel}|/I$ in the red detuned scheme for the initial configuration

$\mathbf{e}_3(0) = \mathbf{S}(0)/S = \mathbf{e}_z$, and $\mathbf{L}(t=0) = \mathbf{0}$. We observe that the induced rotation is always counterclockwise with respect to \mathbf{e}_3 . Thus, an initially clockwise rotating particle will be decelerated. The effects of rotation are only imprinted in the optical power spectrum for high rotation speeds as discussed in the previous section.

VIII. GENERALIZATIONS

In this section we briefly discuss some possible generalizations to the Hamiltonian Eq. (12) of our model.

A. Cotton-Mouton Effect

So far we considered that only the Faraday effect plays a role in optomagnonic coupling. Another effect relevant in several optomagnonic systems is the Cotton-Mouton effect [61, 67], which we now include, discussing its possible impacts on our results.

The Cotton-Mouton (CM) effect is quadratic in the magnetization and is taken into account in the full effective permittivity tensor [103]

$$\varepsilon_{ij}(\mathbf{M}) = \varepsilon_0 \left(\varepsilon \delta_{ij} - i f \sum_k \varepsilon_{ijk} M_k + \sum_{kl} G_{ijkl} M_k M_l \right). \quad (31)$$

Notice that this includes a term $\propto M_k M_l$ which was not included in our previous formalism [cf. Eq. (4)]. For cubic crystals, such as YIG, most of the tensor components G_{ijkl} are zero by symmetry and the non-vanishing ones are [103, 104] $G_{iii} = G_{11}$, $G_{iij} = G_{12}$, $G_{ijj} = G_{44}$ for $i \neq j$ and $i, j \in \{1, 2, 3\}$.

The Hamiltonian obtained by quantizing the CM contribution to the energy density is given by (for details see Appendix G)

$$\begin{aligned} \hat{H}_{\text{int}}^{\text{CM}} = & \hbar g_{\text{CM}}^{44} \left(\hat{S}_z \hat{S}_+ \hat{a}_1^\dagger \hat{a}_2 + \hat{S}_- \hat{S}_z \hat{a}_2^\dagger \hat{a}_1 \right) \\ & + \hbar g_{\text{CM}}^{12} \hat{S}_z^2 (\hat{a}_1^\dagger \hat{a}_1 - \hat{a}_2^\dagger \hat{a}_2), \end{aligned} \quad (32)$$

where we neglected the constant shift in the photon field. The coupling constants g_{CM}^{44} and g_{CM}^{12} are given by

$$\begin{aligned} g_{\text{CM}}^{44} &= \frac{\varepsilon_0}{2\hbar} \left(\frac{M_S}{S} \right)^2 G_{44} \tilde{g}, \\ g_{\text{CM}}^{12} &= \frac{\omega_r}{8\varepsilon} \left(\frac{M_S}{S} \right)^2 (G_{11} - G_{12}), \end{aligned} \quad (33)$$

under the approximation $\int d\mathbf{r} |E_h|^2 \approx \int d\mathbf{r} |E_v|^2 \approx \frac{\hbar\omega_r}{2\varepsilon_0\varepsilon}$.

The equations of motion for the spin and the cavity fields including the additional interacting term Eq. (32)

read

$$\begin{aligned} \dot{\mathbf{S}} &= \tilde{\mathbf{B}}_{\text{eff}} \times \mathbf{S} - 2\omega_D (\mathbf{e}_3 \cdot \mathbf{S}) (\mathbf{e}_3 \times \mathbf{S}) + \tau_G, \\ \dot{a}_1 &= i(\Delta_1 - g_{\text{CM}}^{12} S_z) a_1 - i(g + g_{\text{CM}}^{44} S_z) S_+ a_2 + \varepsilon_{L1} - \frac{1}{2} \kappa a_1, \\ \dot{a}_2 &= i(\Delta_2 + g_{\text{CM}}^{12} S_z) a_2 - i(g + g_{\text{CM}}^{44} S_z) S_- a_1 + \varepsilon_{L2} - \frac{1}{2} \kappa a_2, \end{aligned} \quad (34)$$

where the effective field is now given by $\tilde{\mathbf{B}}_{\text{eff}} = \mathbf{B}_{\text{eff}} + \mathbf{B}_{\text{opt}}^{\text{CM}}$ with

$$\begin{aligned} \mathbf{B}_{\text{opt}}^{\text{CM}} = & g_{\text{CM}}^{44} \begin{pmatrix} (a_1^\dagger a_2 + a_2^\dagger a_1) S_z \\ i(a_1^\dagger a_2 - a_2^\dagger a_1) S_z \\ (a_1^\dagger a_2 + a_2^\dagger a_1) S_x + i(a_1^\dagger a_2 - a_2^\dagger a_1) S_y \end{pmatrix} \\ & - 2g_{\text{CM}}^{12} \begin{pmatrix} (a_1^\dagger a_1 - a_2^\dagger a_2) S_x \\ (a_1^\dagger a_1 - a_2^\dagger a_2) S_y \\ 0 \end{pmatrix}. \end{aligned} \quad (35)$$

For YIG, $G_{44} M_S^2 = -1.14 \cdot 10^{-4}$ and $(G_{11} - G_{12} - 2G_{44}) M_S^2 = 5.73 \cdot 10^{-5}$ [61]. For small deflections of the spin from the z axis, i.e. $S_z \sim S$ and $S_{x,y} \sim 0$, the additional contribution to the optically induced magnetic field is of the same structure and magnitude as the one caused by the Faraday effect, considering that the value of g_{CM}^{44} mainly differs from g given by Eq. (11) by a factor of S^{-1} . Therefore, the inclusion of Cotton-Mouton effect terms do not change qualitatively the results presented in the main text.

B. Anisotropy

Some crystal systems, including YIG, exhibit cubic symmetry for which the magnetocrystalline anisotropy energy can be written as (for a homogeneous material) [45, 60, 105, 106]

$$\begin{aligned} E_c = & K_1 V [(s \cdot \mathbf{e}_1)^2 (s \cdot \mathbf{e}_2)^2 + (s \cdot \mathbf{e}_1)^2 (s \cdot \mathbf{e}_3)^2 \\ & + (s \cdot \mathbf{e}_2)^2 (s \cdot \mathbf{e}_3)^2] + K_2 V (s \cdot \mathbf{e}_1)^2 (s \cdot \mathbf{e}_2)^2 (s \cdot \mathbf{e}_3)^2, \end{aligned} \quad (36)$$

where K_1 and K_2 denote the respective first- and second-order cubic anisotropy constants and $\mathbf{s} = \mathbf{S}/S$. As the term $\propto K_2$ is of 6th order it can be safely neglected. If we assume only small deviations of the spin \mathbf{s} from one of its equilibrium directions, e.g. $\mathbf{s} \cdot \mathbf{e}_3 \sim 1$, and keep the other terms up to second order, Eq. (36) can be approximated as

$$\begin{aligned} E_c \approx & K_1 V [(s \cdot \mathbf{e}_1)^2 + (s \cdot \mathbf{e}_2)^2] \\ & = K_1 V |\mathbf{s} \times \mathbf{e}_3|^2, \end{aligned} \quad (37)$$

where we have used that $\mathbf{e}_3 = \mathbf{e}_1 \times \mathbf{e}_2$ and the vector triple product expansion. By expressing $\sin \phi = |\mathbf{s} \times \mathbf{e}_3|$

and $\cos \phi = \mathbf{s} \cdot \mathbf{e}_3$, ϕ being the angle between \mathbf{s} and \mathbf{e}_3 , the cubic anisotropy term Eq. (37) can be rewritten as

$$E_c \approx K_1 V [1 - (\mathbf{s} \cdot \mathbf{e}_3)^2], \quad (38)$$

which has the same form as the one for uniaxial symmetry apart from a constant shift. Therefore, for small oscillations of the magnetization around one of the directions which minimizes the anisotropy energy density, cubic crystals can be treated to a good approximation as crystals with uniaxial anisotropy, as is often considered for YIG [107–110]. Furthermore, other magnetic oxides, such as those incorporating bismuth, exhibit large uniaxial anisotropies [111].

In case of a non-spherical particle there is an additional source of magnetic anisotropy due to its shape. The shape of the sample generates a demagnetizing field which is not equal in all directions [105]. The energy density of such geometric anisotropy is given by $\mu_0 \mathbf{M} \tilde{N} \mathbf{M} / 2$, where \tilde{N} is the demagnetization. For example, for a prolate spheroid with semi-major axis along the \mathbf{e}_z direction one has $\tilde{N} = \text{diag}[N_T, N_T, 1 - 2N_T]$ with N_T the demagnetization coefficient. A non-spherical shape entails changes not only in the magnetic energy but also in the rotational part of the Hamiltonian. On the one hand, it gives rise to a more complex inertia tensor and on the other hand the electromagnetic fields inside the rotating particle cannot be assumed to be independent of the particle orientation. These effects can be considered to be small if the shape does not deviate much from a sphere.

IX. CONCLUSION

We proposed an optical method to probe the coupled spin-mechanics of levitated magnetic microparticles via optomagnonic effects. We showed that the spin dynamics can be also driven by the optical drive, inducing almost lossless angular oscillations through the spin-mechanics coupling. This coupling between magnetization and angular motion can be probed via the power spectrum of the cavity modes, which exhibit two main resonance peaks at ~ 100 kHz and ~ 2 GHz for micrometer-sized parti-

cles and an applied magnetic field of ~ 60 mT. These are attributed to angular oscillations and spin dynamics that are shifted by the magnetocrystalline anisotropy. We found that due to the damping of the magnetization (Gilbert damping) a rotation of the microparticle around the magnetic anisotropy direction can be optically induced for an initially non-rotating particle. However, the induced angular frequency is low (~ 0.2 μ Hz). We showed that this angular frequency can be increased by adding an oscillatory rf magnetic field perpendicular to the bias magnetic field. In particular, if the drive is at resonance with the shifted spin precession frequency, the aforementioned effects are enhanced and the setup can be used to induce fast rotations of the particle around its magnetic anisotropy axis. This resonant condition can be identified by the appearance of an additional peak in the spectrum.

In general, the optical quality factor of the particle and the supported driving power limit the driven angular motion. In experiments the quality factor will be restricted by additional sources, like surface roughness, and not only by the considered radiative losses. In order to improve the quality factor the system can be modified by placing the particle in an external optical cavity.

We have studied the classical dynamics of the levitated magnetic particle coupled to light, in particular neglecting thermal and shot noise. These, together with the effect of the trapping potential, need to be included in order to study the dynamics in the quantum regime. Experimentally, levitated magnetic particles can provide a unique platform to probe transduction of angular momentum in the quantum regime, and eventually serve as ultrasensitive torque sensors [112, 113].

ACKNOWLEDGEMENTS

We acknowledge funding from the Max Planck Society and from the Deutsche Forschungsgemeinschaft (DFG, German Research Foundation) through Project-ID 429529648-TRR 306 QuCoLiMa ("Quantum Cooperativity of Light and Matter"). V.W. thanks K. Kustura, A. E. Rubio López and C. C. Rusconi for fruitful discussions.

-
- [1] A. Ashkin, *Optical trapping and manipulation of neutral particles using lasers: a reprint volume with commentaries* (World Scientific, 2006).
 - [2] D. G. Grier, A revolution in optical manipulation, *Nature* **424**, 810 (2003).
 - [3] E. Hebestreit, M. Frimmer, R. Reimann, and L. Novotny, Sensing static forces with free-falling nanoparticles, *Phys. Rev. Lett.* **121**, 063602 (2018).
 - [4] G. Ranjit, D. P. Atherton, J. H. Stutz, M. Cunningham, and A. A. Geraci, Attonewton force detection using microspheres in a dual-beam optical trap in high vacuum, *Phys. Rev. A* **91**, 051805 (2015).
 - [5] G. Ranjit, M. Cunningham, K. Casey, and A. A. Geraci, Zeptonewton force sensing with nanospheres in an optical lattice, *Phys. Rev. A* **93**, 053801 (2016).

- [6] A. A. Geraci, S. B. Papp, and J. Kitching, Short-range force detection using optically cooled levitated microspheres, *Phys. Rev. Lett.* **105**, 101101 (2010).
- [7] A. Geraci and H. Goldman, Sensing short range forces with a nanosphere matter-wave interferometer, *Phys. Rev. D* **92**, 062002 (2015).
- [8] D. Hempston, J. Vovrosh, M. Toroš, G. Winstone, M. Rashid, and H. Ulbricht, Force sensing with an optically levitated charged nanoparticle, *Appl. Phys. Lett.* **111**, 133111 (2017).
- [9] C. P. Blakemore, A. D. Rider, S. Roy, Q. Wang, A. Kawasaki, and G. Gratta, Three-dimensional force-field microscopy with optically levitated microspheres, *Phys. Rev. A* **99**, 023816 (2019).
- [10] F. Monteiro, W. Li, G. Afek, C.-l. Li, M. Mossman, and D. C. Moore, Force and acceleration sensing with optically levitated nanogram masses at microkelvin temperatures, *Phys. Rev. A* **101**, 053835 (2020).
- [11] F. Monteiro, S. Ghosh, A. G. Fine, and D. C. Moore, Optical levitation of 10-ng spheres with nano-g acceleration sensitivity, *Phys. Rev. A* **96**, 063841 (2017).
- [12] D. S. Bykov, O. A. Schmidt, T. G. Euser, and P. S. J. Russell, Flying particle sensors in hollow-core photonic crystal fibre, *Nature Photonics* **9**, 461 (2015).
- [13] R. Zeltner, R. Pennetta, S. Xie, and P. S. Russell, Flying particle microlaser and temperature sensor in hollow core photonic crystal fiber, *Optics Letters* **43**, 1479 (2018).
- [14] Y. Zhang, P. Liang, Z. Liu, J. Lei, J. Yang, and L. Yuan, A novel temperature sensor based on optical trapping technology, *Journal of Lightwave Technology* **32**, 1394 (2014).
- [15] A. Ashkin, J. M. Dziedzic, and T. Yamane, Optical trapping and manipulation of single cells using infrared laser beams, *Nature* **330**, 769 (1987).
- [16] A. Ashkin and J. M. Dziedzic, Optical trapping and manipulation of viruses and bacteria, *Science* **235**, 1517 (1987).
- [17] M. J. Lang and S. M. Block, Resource letter: Lbot-I: Laser-based optical tweezers, *American Journal of Physics* **71**, 201 (2003).
- [18] K. C. Neuman and S. M. Block, Optical trapping, *Review of Scientific Instruments* **75**, 2787 (2004).
- [19] O. M. Maragò, P. H. Jones, P. G. Gucciardi, G. Volpe, and A. C. Ferrari, Optical trapping and manipulation of nanostructures, *Nature Nanotechnology* **8**, 807 (2013).
- [20] J. Gieseler, L. Novotny, and R. Quidant, Thermal nonlinearities in a nanomechanical oscillator, *Nature Physics* **9**, 806 (2013).
- [21] J. Gieseler, R. Quidant, C. Dellago, and L. Novotny, Dynamic relaxation of a levitated nanoparticle from a non-equilibrium steady state, *Nature Nanotechnology* **9**, 358 (2014).
- [22] J. Millen, T. Deesuwan, P. Barker, and J. Anders, Nanoscale temperature measurements using non-equilibrium brownian dynamics of a levitated nanosphere, *Nature Nanotechnology* **9**, 425 (2014).
- [23] F. Ricci, R. A. Rica, M. Spasenović, J. Gieseler, L. Rondin, L. Novotny, and R. Quidant, Optically levitated nanoparticle as a model system for stochastic bistable dynamics, *Nat. Comm.* **8**, 1 (2017).
- [24] Y. Arita, M. Mazilu, and K. Dholakia, Laser-induced rotation and cooling of a trapped microgyroscope in vacuum, *Nat. Comm.* **4**, 2374 (2013).
- [25] E. Hebestreit, R. Reimann, M. Frimmer, and L. Novotny, Measuring the internal temperature of a levitated nanoparticle in high vacuum, *Phys. Rev. A* **97**, 043803 (2018).
- [26] T. M. Hoang, Y. Ma, J. Ahn, J. Bang, F. Robicheaux, Z.-Q. Yin, and T. Li, Torsional optomechanics of a levitated nonspherical nanoparticle, *Phys. Rev. Lett.* **117**, 123604 (2016).
- [27] M. Rashid, M. Toroš, A. Setter, and H. Ulbricht, Precession motion in levitated optomechanics, *Phys. Rev. Lett.* **121**, 253601 (2018).
- [28] U. c. v. Delić, M. Reisenbauer, D. Grass, N. Kiesel, V. Vuletić, and M. Aspelmeyer, Cavity cooling of a levitated nanosphere by coherent scattering, *Phys. Rev. Lett.* **122**, 123602 (2019).
- [29] D. Windey, C. Gonzalez-Ballester, P. Maurer, L. Novotny, O. Romero-Isart, and R. Reimann, Cavity-based 3d cooling of a levitated nanoparticle via coherent scattering, *Phys. Rev. Lett.* **122**, 123601 (2019).
- [30] F. Tebbenjohanns, M. Frimmer, A. Militaru, V. Jain, and L. Novotny, Cold damping of an optically levitated nanoparticle to microkelvin temperatures, *Phys. Rev. Lett.* **122**, 223601 (2019).
- [31] G. P. Conangla, F. Ricci, M. T. Cuairan, A. W. Schell, N. Meyer, and R. Quidant, Optimal feedback cooling of a charged levitated nanoparticle with adaptive control, *Phys. Rev. Lett.* **122**, 223602 (2019).
- [32] J. Gieseler, B. Deutsch, R. Quidant, and L. Novotny, Subkelvin parametric feedback cooling of a laser-trapped nanoparticle, *Phys. Rev. Lett.* **109**, 103603 (2012).
- [33] T. Li, S. Kheifets, and M. G. Raizen, Millikelvin cooling of an optically trapped microsphere in vacuum (Nature Publishing Group, 2011) pp. 527–530.
- [34] R. Reimann, M. Doderer, E. Hebestreit, R. Diehl, M. Frimmer, D. Windey, F. Tebbenjohanns, and L. Novotny, Ghz rotation of an optically trapped nanoparticle in vacuum, *Phys. Rev. Lett.* **121**, 033602 (2018).
- [35] J. Ahn, Z. Xu, J. Bang, Y.-H. Deng, T. M. Hoang, Q. Han, R.-M. Ma, and T. Li, Optically levitated nanodumbbell torsion balance and ghz nanomechanical rotor, *Phys. Rev. Lett.* **121**, 033603 (2018).
- [36] D. E. Chang, C. Regal, S. Papp, D. Wilson, J. Ye, O. Painter, H. J. Kimble, and P. Zoller, Cavity optomechanics using an optically levitated nanosphere, *Proceedings of the National Academy of Sciences* **107**, 1005 (2010).
- [37] O. Romero-Isart, A. C. Pflanzer, M. L. Juan, R. Quidant, N. Kiesel, M. Aspelmeyer, and J. I. Cirac, Optically levitating dielectrics in the quantum regime: Theory and protocols, *Phys. Rev. A* **83**, 013803 (2011).
- [38] O. Romero-Isart, M. L. Juan, R. Quidant, and J. I. Cirac, Toward quantum superposition of living organisms, *New Journal of Physics* **12**, 033015 (2010).
- [39] J. Bateman, S. Nimmrichter, K. Hornberger, and H. Ulbricht, Near-field interferometry of a free-falling

- nanoparticle from a point-like source, *Nat. Comm.* **5**, 1 (2014).
- [40] M. Scala, M. Kim, G. Morley, P. Barker, and S. Bose, Matter-wave interferometry of a levitated thermal nanoscillator induced and probed by a spin, *Phys. Rev. Lett.* **111**, 180403 (2013).
- [41] L. Magrini, P. Rosenzweig, C. Bach, A. Deutschmann-Olek, S. G. Hofer, S. Hong, N. Kiesel, A. Kugi, and M. Aspelmeyer, Real-time optimal quantum control of mechanical motion at room temperature, *Nature* **595**, 373 (2021).
- [42] F. Tebbenjohanns, M. L. Mattana, M. Rossi, M. Frimmer, and L. Novotny, Quantum control of a nanoparticle optically levitated in cryogenic free space, *Nature* **595**, 378 (2021).
- [43] A. Einstein and W. De Haas, Experimental proof of the existence of amperes molecular currents, in *Proc. KNAW*, Vol. 181 (1915) p. 696.
- [44] S. J. Barnett, Magnetization by rotation, *Phys. Rev.* **6**, 239 (1915).
- [45] S. Chikazumi and C. D. Graham, *Physics of Ferromagnetism*, 94 (Oxford University Press, 2009).
- [46] O. Romero-Isart, L. Clemente, C. Navau, A. Sanchez, and J. Cirac, Quantum magnetomechanics with levitating superconducting microspheres, *Phys. Rev. Lett.* **109**, 147205 (2012).
- [47] T. Wang, S. Lourette, S. R. O’Kelley, M. Kayci, Y. Band, D. F. J. Kimball, A. O. Sushkov, and D. Budker, Dynamics of a ferromagnetic particle levitated over a superconductor, *Phys. Rev. Appl.* **11**, 044041 (2019).
- [48] C. Timberlake, G. Gasbarri, A. Vinante, A. Setter, and H. Ulbricht, Acceleration sensing with magnetically levitated oscillators above a superconductor, *Appl. Phys. Lett.* **115**, 224101 (2019).
- [49] C. W. Lewandowski, T. D. Knowles, Z. B. Etienne, and B. D’Urso, High-sensitivity accelerometry with a feedback-cooled magnetically levitated microsphere, *Phys. Rev. Appl.* **15**, 014050 (2021).
- [50] B. R. Slezak, C. W. Lewandowski, J.-F. Hsu, and B. D’Urso, Cooling the motion of a silica microsphere in a magneto-gravitational trap in ultra-high vacuum, *New Journal of Physics* **20**, 063028 (2018).
- [51] J.-F. Hsu, P. Ji, C. W. Lewandowski, and B. D’Urso, Cooling the motion of diamond nanocrystals in a magneto-gravitational trap in high vacuum, *Scientific Reports* **6**, 1 (2016).
- [52] J. Prat-Camps, C. Teo, C. Rusconi, W. Wiczorek, and O. Romero-Isart, Ultrasensitive inertial and force sensors with diamagnetically levitated magnets, *Phys. Rev. Appl.* **8**, 034002 (2017).
- [53] J. Gieseler, A. Kabcenell, E. Rosenfeld, J. Schaefer, A. Safira, M. J. Schuetz, C. Gonzalez-Ballester, C. C. Rusconi, O. Romero-Isart, and M. D. Lukin, Single-spin magnetomechanics with levitated micromagnets, *Phys. Rev. Lett.* **124**, 163604 (2020).
- [54] M. O’Brien, S. Dunn, J. Downes, and J. Twamley, Magneto-mechanical trapping of micro-diamonds at low pressures, *Appl. Phys. Lett.* **114**, 053103 (2019).
- [55] J. Houlton, M. Chen, M. Brubaker, K. Bertness, and C. Rogers, Axisymmetric scalable magnetogravitational trap for diamagnetic particle levitation, *Review of Scientific Instruments* **89**, 125107 (2018).
- [56] M. T. Johnsson, G. K. Brennen, and J. Twamley, Macroscopic superpositions and gravimetry with quantum magnetomechanics, *Scientific Reports* **6**, 1 (2016).
- [57] M. Cirio, G. Brennen, and J. Twamley, Quantum magnetomechanics: ultrahigh-q-levitated mechanical oscillators, *Phys. Rev. Lett.* **109**, 147206 (2012).
- [58] A. Vinante, P. Falferi, G. Gasbarri, A. Setter, C. Timberlake, and H. Ulbricht, Ultralow mechanical damping with meissner-levitated ferromagnetic microparticles, *Phys. Rev. Appl.* **13**, 064027 (2020).
- [59] M. Perdriat, C. Pellet-Mary, P. Huillery, L. Rondin, and G. Hétet, Spin-mechanics with nitrogen-vacancy centers and trapped particles, *Micromachines* **12**, 651 (2021).
- [60] L. Landau, L. Pitaevskii, and E. Lifshitz, *Electrodynamics of Continuous Media, volume 8 of* (Butterworth-Heinemann, 1984).
- [61] D. D. Stancil and A. Prabhakar, *Spin waves*, Vol. 5 (Springer, 2009).
- [62] S. Viola Kusminskiy, H. X. Tang, and F. Marquardt, Coupled spin-light dynamics in cavity optomagnonics, *Phys. Rev. A* **94** (2016).
- [63] T. Liu, X. Zhang, H. X. Tang, and M. E. Flatté, Optomagnonics in magnetic solids, *Phys. Rev. B* **94**, 060405 (2016).
- [64] S. Sharma, Y. M. Blanter, and G. E. Bauer, Light scattering by magnons in whispering gallery mode cavities, *Phys. Rev. B* **96**, 094412 (2017).
- [65] E. Almpanis, Dielectric magnetic microparticles as photomagnonic cavities: Enhancing the modulation of near-infrared light by spin waves, *Phys. Rev. B* **97**, 184406 (2018).
- [66] E. Almpanis, G. Zouros, P. Pantazopoulos, K. Tsakmakidis, N. Papanikolaou, and N. Stefanou, Spherical optomagnonic microresonators: Triple-resonant photon transitions between zeeman-split mie modes, *Phys. Rev. B* **101**, 054412 (2020).
- [67] A. Osada, A. Gloppe, Y. Nakamura, and K. Usami, Orbital angular momentum conservation in brillouin light scattering within a ferromagnetic sphere, *New Journal of Physics* **20**, 103018 (2018).
- [68] S. V. Kusminskiy, Cavity optomagnonics (2019), [arXiv:1911.11104](https://arxiv.org/abs/1911.11104).
- [69] J. A. Haigh, A. Nunnenkamp, A. J. Ramsay, and A. J. Ferguson, Triple-resonant brillouin light scattering in magneto-optical cavities, *Phys. Rev. Lett.* **117**, 133602 (2016).
- [70] J. Haigh, N. Lambert, S. Sharma, Y. Blanter, G. Bauer, and A. Ramsay, Selection rules for cavity-enhanced brillouin light scattering from magnetostatic modes, *Phys. Rev. B* **97**, 214423 (2018).
- [71] A. Osada, R. Hisatomi, A. Noguchi, Y. Tabuchi, R. Yamazaki, K. Usami, M. Sadgrove, R. Yalla, M. Nomura, and Y. Nakamura, Cavity optomagnonics with spin-orbit coupled photons, *Phys. Rev. Lett.* **116**, 223601 (2016).
- [72] A. Osada, A. Gloppe, R. Hisatomi, A. Noguchi, R. Yamazaki, M. Nomura, Y. Nakamura, and K. Usami, Brillouin light scattering by magnetic quasivortices in cavity

- optomagnonics, *Phys. Rev. Lett.* **120**, 133602 (2018).
- [73] X. Zhang, N. Zhu, C.-L. Zou, and H. X. Tang, Optomagnonic whispering gallery microresonators, *Phys. Rev. Lett.* **117**, 123605 (2016).
- [74] B. Z. Rameshti, S. V. Kusminskiy, J. A. Haigh, K. Usami, D. Lachance-Quirion, Y. Nakamura, C.-M. Hu, H. X. Tang, G. E. W. Bauer, and Y. M. Blanter, Cavity magnonics (2021), [arXiv:2106.09312](https://arxiv.org/abs/2106.09312).
- [75] J. Heebner, R. Grover, T. Ibrahim, and T. A. Ibrahim, *Optical Microresonators: Theory, Fabrication, and Applications*, Vol. 138 (Springer Science & Business Media, 2008).
- [76] C. F. Bohren and D. R. Huffman, *Absorption and scattering of light by small particles* (John Wiley & Sons, 2008).
- [77] A. I. Kuznetsov, A. E. Miroschnichenko, M. L. Brongersma, Y. S. Kivshar, and B. Lukyanchuk, Optically resonant dielectric nanostructures, *Science* **354** (2016).
- [78] G. W. Ford and S. A. Wener, Scattering and absorption of electromagnetic waves by a gyrotropic sphere, *Phys. Rev. B* **18**, 6752 (1978).
- [79] P. Fleury and R. Loudon, Scattering of light by one- and two-magnon excitations, *Physical Review* **166**, 514 (1968).
- [80] T. A. Nieminen, N. R. Heckenberg, and H. Rubinsztein-Dunlop, Optical measurement of microscopic torques, *Journal of Modern Optics* **48**, 405 (2001).
- [81] M. E. Friese, T. A. Nieminen, N. R. Heckenberg, and H. Rubinsztein-Dunlop, Optical alignment and spinning of laser-trapped microscopic particles, *Nature* **394**, 348 (1998).
- [82] S. H. Simpson, D. C. Benito, and S. Hanna, Polarization-induced torque in optical traps, *Phys. Rev. A* **76**, 043408 (2007).
- [83] M. Donato, A. Mazzulla, P. Pagliusi, A. Magazzù, R. Hernandez, C. Provenzano, P. Gucciardi, O. Maragò, and G. Cipparrone, Light-induced rotations of chiral birefringent microparticles in optical tweezers, *Scientific Reports* **6**, 1 (2016).
- [84] T. L. Gilbert, A phenomenological theory of damping in ferromagnetic materials, *IEEE Transactions on Magnetics* **40**, 3443 (2004).
- [85] A. Antonov, A. Agranovskaya, G. Petrova, and A. Titova, Optical properties of yttrium-iron garnet, *Journal of Applied Spectroscopy* **11**, 1225 (1969).
- [86] D. Gatteschi, R. Sessoli, and J. Villain, *Molecular Nanomagnets*, Vol. 1 (Oxford University Press, 2006).
- [87] C. C. Rusconi, V. Pöchlacker, K. Kustura, J. I. Cirac, and O. Romero-Isart, Quantum spin stabilized magnetic levitation, *Phys. Rev. Lett.* **119**, 167202 (2017).
- [88] S. V. Kusminskiy, *Quantum Magnetism, Spin Waves, and Optical Cavities* (Springer, 2019).
- [89] M. Wu and A. Hoffmann, *Recent advances in magnetic insulators-from spintronics to microwave applications* (Academic Press, 2013).
- [90] For instance, one could consider individual driving terms at different frequencies for each mode, which would require additional unitary transformations to a rotating frame in which \hat{H} is time-independent.
- [91] C. W. Gardiner and M. J. Collett, Input and output in damped quantum systems: Quantum stochastic differential equations and the master equation, *Phys. Rev. A* **31**, 3761 (1985).
- [92] J. Buck and H. Kimble, Optimal sizes of dielectric microspheres for cavity qed with strong coupling, *Phys. Rev. A* **67**, 033806 (2003).
- [93] H. Keshtgar, S. Streib, A. Kamra, Y. M. Blanter, and G. E. Bauer, Magnetomechanical coupling and ferromagnetic resonance in magnetic nanoparticles, *Phys. Rev. B* **95**, 134447 (2017).
- [94] Y. Band, Y. Avishai, and A. Shnirman, Dynamics of a magnetic needle magnetometer: Sensitivity to landaulifshitz-gilbert damping, *Phys. Rev. Lett.* **121**, 160801 (2018).
- [95] For YIG particles of $\sim (1\mu\text{m})^3$, this approximation is justified as $\eta_G/S < 10^{-14}$.
- [96] H. Suhl, The theory of ferromagnetic resonance at high signal powers, *Journal of Physics and Chemistry of Solids* **1**, 209 (1957).
- [97] U. Fano, Effects of configuration interaction on intensities and phase shifts, *Phys. Rev.* **124**, 1866 (1961).
- [98] X.-Y. Wang, L.-G. Si, X.-H. Lu, and Y. Wu, Optomechanically tuned fano resonance and slow light in a quadratically coupled optomechanical system with membranes, *Journal of Physics B: Atomic, Molecular and Optical Physics* **53**, 235402 (2020).
- [99] K. Qu and G. Agarwal, Fano resonances and their control in optomechanics, *Phys. Rev. A* **87**, 063813 (2013).
- [100] C. Kittel, On the theory of ferromagnetic resonance absorption, *Physical Review* **73**, 155 (1948).
- [101] Y. Tabuchi, S. Ishino, A. Noguchi, T. Ishikawa, R. Yamazaki, K. Usami, and Y. Nakamura, Quantum magnonics: The magnon meets the superconducting qubit, *Comptes Rendus Physique* **17**, 729 (2016).
- [102] D. Lachance-Quirion, Y. Tabuchi, S. Ishino, A. Noguchi, T. Ishikawa, R. Yamazaki, and Y. Nakamura, Resolving quanta of collective spin excitations in a millimeter-sized ferromagnet, *Science Advances* **3**, e1603150 (2017).
- [103] W. Wettling, M. Cottam, and J. Sandercock, The relation between one-magnon light scattering and the complex magneto-optic effects in yig, *Journal of Physics C: Solid State Physics* **8**, 211 (1975).
- [104] R. Pisarev, I. Sinii, N. Kolpakova, and Y. M. Yakovlev, Magnetic birefringence of light in iron garnets, *Sov. Phys. JETP* **33**, 1175 (1971).
- [105] B. D. Cullity and C. D. Graham, *Introduction to magnetic materials, 2nd Edition* (Wiley-IEEE Press, 2008).
- [106] G. F. Dionne, Anisotropy and magnetoelastic properties, in *Magnetic Oxides* (Springer, 2009) pp. 201–271.
- [107] S. Streib, H. Keshtgar, and G. E. Bauer, Damping of magnetization dynamics by phonon pumping, *Phys. Rev. Lett.* **121**, 027202 (2018).
- [108] M. Elyasi, Y. M. Blanter, and G. E. Bauer, Resources of nonlinear cavity magnonics for quantum information, *Phys. Rev. B* **101**, 054402 (2020).
- [109] A. Pacewicz, J. Krupka, B. Salski, P. Aleshkevych, and P. Kopyt, Rigorous broadband study of the intrinsic ferromagnetic linewidth of monocrystalline garnet spheres, *Scientific Reports* **9**, 1 (2019).

- [110] P. Rijniere, H. Logmans, R. Metselaar, and W. Stacy, Optical measurement of magnetic anisotropy in thin garnet films, *Applied Physics* **8**, 143 (1975).
- [111] P. Hansen, C.-P. Klages, J. Schuldt, and K. Witter, Magnetic and magneto-optical properties of bismuth-substituted lutetium iron garnet films, *Phys. Rev. B* **31**, 5858 (1985).
- [112] A. La Porta and M. D. Wang, Optical torque wrench: Angular trapping, rotation, and torque detection of quartz microparticles, *Phys. Rev. Lett.* **92**, 190801 (2004).
- [113] J. Ahn, Z. Xu, J. Bang, P. Ju, X. Gao, and T. Li, Ultrasensitive torque detection with an optically levitated nanorotor, *Nature Nanotechnology* **15**, 89 (2020).
- [114] V. Datsyuk, Some characteristics of resonant electromagnetic modes in a dielectric sphere, *Appl. Phys. B* **54**, 184 (1992).
- [115] L. A. Weinstein, *Open resonators and open waveguides* (Golem Press, 1969).
- [116] A. R. Edmonds, *Angular momentum in quantum mechanics*, Vol. 4 (Princeton university press, 1996).
- [117] C. C. Rusconi and O. Romero-Isart, Magnetic rigid rotor in the quantum regime: Theoretical toolbox, *Phys. Rev. B* **93**, 054427 (2016).

Appendix A: Decay Rate and Q Factor

In order to calculate the decay rate for the optical modes we need to find the resonance location, i.e. the eigenmodes that are determined by the roots of a characteristic equation. This characteristic equation is obtained by satisfying the boundary conditions at the surface of the microsphere, which implies that the components of the electromagnetic fields inside and outside the sphere match. The resulting equation can be reduced to [92]

$$\frac{j_{l-1}(kR)}{j_l(kR)} - \frac{1}{n} \frac{h_{l-1}^{(1)}(kR/n)}{h_l^{(1)}(kR/n)} = 0 \quad (\text{A1})$$

for TE modes and to

$$\frac{j_{l-1}(kR)}{j_l(kR)} - n \frac{h_{l-1}^{(1)}(kR/n)}{h_l^{(1)}(kR/n)} + \frac{n^2 l}{kR} - \frac{l}{kR} = 0 \quad (\text{A2})$$

for TM modes, where $j_l(x)$ and $h_l^{(1)}(x)$ are the spherical Bessel and Hankel function of first kind and $k = 2\pi n/\lambda_0$ is the wave vector inside the sphere with refractive index n and vacuum laser wavelength λ_0 . We determine the relevant angular mode number by $l = 2\pi nR/\lambda_0$. From the complex roots k_ρ we then obtain the resonance frequency $\omega_r = \text{Re}\{k_\rho c/(nR)\}$ and the decay rate $\kappa = |\text{Im}\{k_\rho c/(nR)\}|$. For large mode numbers l an approximate analytic expression for the complex resonance frequency was derived [114, 115]

$$\omega_\rho = \frac{c}{nR} \left[l + \frac{1}{2} - (t_p^0 + \Delta t_l) \xi \right], \quad (\text{A3})$$

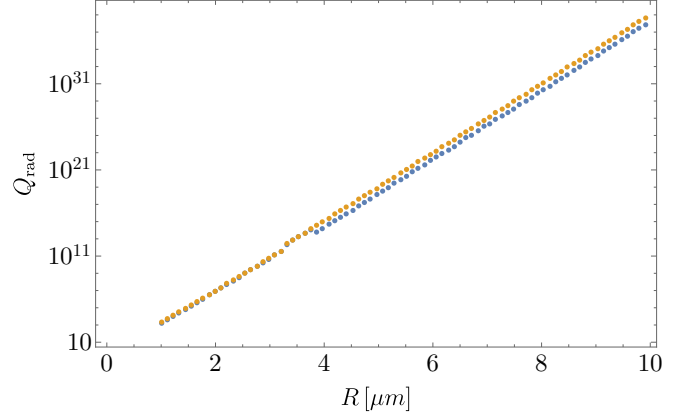


Figure 9. Semi-log plot of the radiative Q factor as a function of the size of the particle R for TE modes (for $\lambda_0 = 1500$ nm and $n = 2.2$). The blue dots depict the solutions obtained from numerically solving the characteristic equation Eq. (A2), whereas the orange ones represent the approximated Q factor Eq. (A5).

where

$$\Delta t_l = n^{1-2b} \frac{1 + ie^{-2T_l}}{\xi \sqrt{n^2 - 1}},$$

$$T_l = \left(l + \frac{1}{2} \right) (\eta_l - \tanh(\eta_l)),$$

$$\eta_l = \text{arccosh} \left[n \left[1 - \frac{1}{l + \frac{1}{2}} \left(t_p^0 \xi + \frac{l^{1-2b}}{\sqrt{l^2 - 1}} \right) \right]^{-1} \right],$$

$$\xi = \left[\frac{1}{2} \left(l + \frac{1}{2} \right) \right]^{1/3},$$

and

$$b = \begin{cases} 0 & \text{TE modes} \\ 1 & \text{TM modes.} \end{cases}$$

Also, t_p^0 denotes the p th zero of the Airy function, where p corresponds to the radial mode number. Note that we only consider $p = 1$ modes [92] and focus on TE modes for our calculations.

The Q factor due to radiative loss can be obtained through the characteristic equation as

$$Q_{\text{rad}} = \frac{\text{Re}\{k_\rho\}}{2|\text{Im}\{k_\rho\}|}. \quad (\text{A4})$$

Using Eq. (A3) to calculate the Q factor leads to

$$Q_{\text{rad}}^{\text{approx}} = \frac{1}{2} \left(l + \frac{1}{2} \right) n^{-(1-2b)} (n^2 - 1)^{1/2} e^{2T_1}, \quad (\text{A5})$$

where we used $|(t_p^0 + \Delta t_l)\xi| \ll l + \frac{1}{2}$ [114]. In Fig. 9 we show the dependence of the Q factor on the radius of the particle. As the magnitude of the exact and the approximated solutions match, we use Eq. (A3) to obtain the values for ω_r and κ_{rad} in our simulations of the

trajectories, namely,

$$\omega_r = \frac{c}{nR} \left(l + \frac{1}{2} \right) \quad (\text{A6})$$

and

$$\kappa_{\text{rad}} = \frac{c}{nR} \left[\frac{n^{1-2b}}{\sqrt{n^2 - 1}} e^{-2T_1} \right]. \quad (\text{A7})$$

Appendix B: Transition Amplitude

For one magnon absorption the transition amplitude in Eq. (11) can be approximated as [66]

$$\tilde{g} = \frac{-\hbar\omega_r \sqrt{(l - m_i)(l + m_i + 1)}}{\varepsilon_0 \varepsilon l(l + 1)} \left[\frac{(2l + 1)^2 [j_l^2(x) - j_{l-1}(x)j_{l+1}(x)]}{(2l + 1)^2 j_l^2(x) - 4l(l + 1)j_{l-1}(x)j_{l+1}(x) + (l + 1)j_{l-1}^2(x) - lj_{l+1}^2(x)} \right]_{x=k_r R}, \quad (\text{B1})$$

with $k_r = \omega_r n/c$. Note that the absolute value of the transition amplitude for one magnon emission from mode $m_i + 1$ to m_i is the same as the one for absorption from m_i to $m_i + 1$. We consider TE modes and choose $m_i = 0$ such that the coupling strength is maximized, which can be seen in Fig. 10 where the optomagnonic coupling is depicted as a function of m_i .

Appendix C: Commutation Relations

The rotation matrix is given by

$$R(\hat{\Omega}) = \begin{pmatrix} \cos \hat{\gamma} & \sin \hat{\gamma} & 0 \\ -\sin \hat{\gamma} & \cos \hat{\gamma} & 0 \\ 0 & 0 & 1 \end{pmatrix} \begin{pmatrix} \cos \hat{\beta} & 0 & -\sin \hat{\beta} \\ 0 & 1 & 0 \\ \sin \hat{\beta} & 0 & \cos \hat{\beta} \end{pmatrix} \quad (\text{C1})$$

$$\begin{pmatrix} \cos \hat{\alpha} & \sin \hat{\alpha} & 0 \\ -\sin \hat{\alpha} & \cos \hat{\alpha} & 0 \\ 0 & 0 & 1 \end{pmatrix}$$

and its elements commute with the spin operator. The anisotropy axis in the laboratory frame reads

$$\mathbf{e}_3(\hat{\Omega}) = R_{31}(\hat{\Omega})\mathbf{e}_x + R_{32}(\hat{\Omega})\mathbf{e}_y + R_{33}(\hat{\Omega})\mathbf{e}_z. \quad (\text{C2})$$

From the Hamiltonian in Eq. (12) we obtain the coupled Heisenberg equations of motion for the set of operators $\hat{\xi} = (\hat{\mathbf{e}}_3, \hat{\mathbf{L}}, \hat{\mathbf{S}}, \hat{a}_1, \hat{a}_1^\dagger, \hat{a}_2, \hat{a}_2^\dagger)$ by using the following com-

mutation relations [116, 117]

$$\begin{aligned} [\hat{L}_j, \hat{L}_k] &= i\epsilon_{jkl}\hat{L}_l, \\ [\hat{S}_j, \hat{S}_k] &= i\epsilon_{jkl}\hat{S}_l, \\ [\hat{L}_j, R_{kl}(\hat{\Omega})] &= i\epsilon_{jlr}R_{kr}(\hat{\Omega}), \end{aligned}$$

and $[\hat{L}_j, \hat{S}_k] = [\hat{S}_j, R_{kl}(\hat{\Omega})] = [R_{jk}(\hat{\Omega}), R_{lr}(\hat{\Omega})] = 0$. For the cavity operators the usual bosonic commutation relations hold, i.e. $[\hat{a}_i, \hat{a}_j^\dagger] = \delta_{ij}$, $[\hat{a}_i, \hat{a}_i] = [\hat{a}_i^\dagger, \hat{a}_i^\dagger] = 0$. Further, we focus on the classical limit in which the operators are replaced by their expectation values and we neglect any kind of quantum correlations, i.e. $\langle \hat{\xi}_i \hat{\xi}_j \rangle \simeq \langle \hat{\xi}_i \rangle \langle \hat{\xi}_j \rangle \forall i, j$. The set of Heisenberg equations of motion $\frac{d\hat{\xi}}{dt} = \Xi(\hat{\xi})$ is therefore approximated by the closed set of semiclassical equations $\frac{d\langle \hat{\xi} \rangle}{dt} = \Xi(\langle \hat{\xi} \rangle)$, where Ξ is a vector function of $\hat{\xi}$.

Appendix D: Derivation of the Optomagnonic Steady State

In what follows we drop the bar-notation for the steady state. For the steady state of the optical field we need to

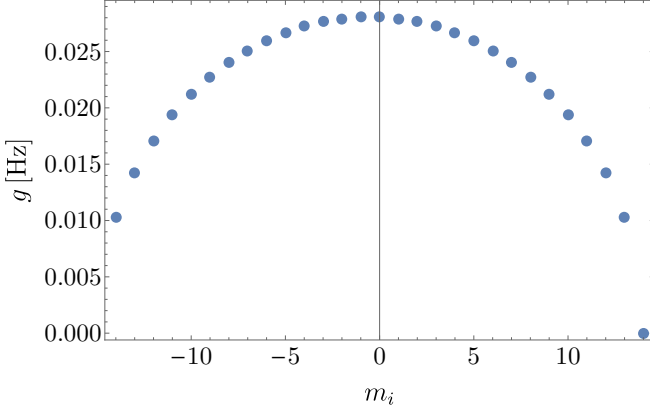


Figure 10. Optomagnonic coupling strength g for triple-resonant photon transition from mode m_i to $m_i + 1$ for a sphere of radius $R = 1.5 \mu\text{m}$.

solve:

$$\begin{aligned}
 -ig(S_+ a_1^\dagger a_2 - S_- a_2^\dagger a_1) &= 0 \\
 \frac{\omega_B}{2} S_+ + g S_z a_2^* a_1 &= 0 \\
 i\Delta_1 a_1 - ig S_+ a_2 + \epsilon_{L1} - \frac{1}{2} \kappa a_1 &= 0 \\
 i\Delta_2 a_2 - ig S_- a_1 + \epsilon_{L2} - \frac{1}{2} \kappa a_2 &= 0 \quad (\text{D1})
 \end{aligned}$$

Note, that here we describe the equations for \mathbf{S} in terms of the ladder operators, such that $\dot{S}_z = -ig(S_+ a_1^\dagger a_2 - S_- a_2^\dagger a_1) - \dot{L}_z$ and $\dot{S}_+ = -i\omega_B S_+ - 2ig S_z a_2^\dagger a_1 - \dot{L}_+$. From the second equation of Eq. (D1) we get

$$S_+ = -\frac{2g}{\omega_B} a_2^* a_1 S_z.$$

As $S_- S_+ = S_x^2 + S_y^2 = S^2 - S_z^2$, we multiply the above equation by $S_- = S_+^*$, such that $S^2 - S_z^2 = \frac{4g^2}{\omega_B^2} |a_1|^2 |a_2|^2 S_z^2$, which results in

$$S_z = \frac{S}{\sqrt{1 + \frac{4g^2}{\omega_B^2} |a_1|^2 |a_2|^2}} \quad (\text{D2})$$

and

$$S_+ = -\frac{2g a_2^* a_1 S}{\sqrt{\omega_B^2 + 4g^2 |a_1|^2 |a_2|^2}}. \quad (\text{D3})$$

This allows us to rewrite the last two equations in Eq. (D1) as

$$\begin{aligned}
 i\Delta_1 a_1 + i \frac{2g^2 |a_2|^2 a_1 S}{\sqrt{\omega_B^2 + 4g^2 |a_1|^2 |a_2|^2}} + \epsilon_{L1} - \frac{1}{2} \kappa a_1 &= 0 \\
 i\Delta_2 a_2 + i \frac{2g^2 a_2 |a_1|^2 S}{\sqrt{\omega_B^2 + 4g^2 |a_1|^2 |a_2|^2}} + \epsilon_{L2} - \frac{1}{2} \kappa a_2 &= 0, \quad (\text{D4})
 \end{aligned}$$

which is a set of coupled equations that involves only the cavity fields, although being nonlinear. If for instance $\epsilon_{L2} = 0$, then the second equation reads

$$i\Delta_2 a_2 + i \frac{2g^2 a_2 |a_1|^2 S}{\sqrt{\omega_B^2 + 4g^2 |a_1|^2 |a_2|^2}} - \frac{1}{2} \kappa a_2 = 0$$

and multiplying it by a_2^* results in

$$i\Delta_2 |a_2|^2 + i \frac{2g^2 |a_2|^2 |a_1|^2 S}{\sqrt{\omega_B^2 + 4g^2 |a_1|^2 |a_2|^2}} = \frac{1}{2} \kappa |a_2|^2.$$

Note that the LHS is purely imaginary while the RHS is purely real, which implies that the only possible solution for this equation is $|a_2|^2 = 0$. From this it follows in turn that $a_1 = -\frac{\epsilon_{L1}}{i\Delta_1 - \frac{1}{2}\kappa}$, $S_z = S$, $S_+ = S_- = S_x = S_y = 0$. In order to get a spin steady state that is affected by light it is necessary to also pump mode 2, i.e. $\epsilon_{L2} \neq 0$.

In the limit $\omega_B \gg 4g|a_1||a_2|$, Eq. (D4) reduces to

$$\begin{aligned}
 i\Delta_1 a_1 + i \frac{2g^2 |a_2|^2 a_1 S}{\omega_B} + \epsilon_{L1} - \frac{1}{2} \kappa a_1 &= 0 \\
 i\Delta_2 a_2 + i \frac{2g^2 a_2 |a_1|^2 S}{\omega_B} + \epsilon_{L2} - \frac{1}{2} \kappa a_2 &= 0, \quad (\text{D5})
 \end{aligned}$$

such that

$$a_1 = -\frac{\epsilon_{L1}}{i\left(\Delta_1 + \frac{2g^2 |a_2|^2 S}{\omega_B}\right) - \frac{1}{2}\kappa} \quad (\text{D6})$$

and

$$\begin{aligned}
 i\Delta_2 a_2 + i \frac{2g^2 S}{\gamma B} \frac{\epsilon_{L1}^2}{\left(\Delta_1 + \frac{2g^2 |a_2|^2 S}{\omega_B}\right)^2 + \frac{1}{4}\kappa^2} a_2 \\
 - \frac{1}{2} \kappa a_2 + \epsilon_{L2} = 0. \quad (\text{D7})
 \end{aligned}$$

Appendix E: Further Dynamics

If the particle is initially unmagnetized and non-rotating, then switching on the magnetic field induces a rotational motion, as a change of magnetization results in mechanical rotation. This is due to conservation of angular momentum, as stated by the Einstein-de Haas effect [43]. The relation between magnetization and mechanical angular momentum is given by

$$\Delta M V = -\gamma \Delta L. \quad (\text{E1})$$

In our case $\Delta M = M_S$, thus, the resulting rotation frequency is $\omega_{\text{rot}}/(2\pi) \approx 30 \text{ Hz}$. In Fig. 11 we show the evolution of \mathbf{e}_3 in the xy plane in the red detuning scheme for $\mathbf{e}_3(0) = \mathbf{S}(0)/S = \mathbf{e}_z$ and (a) $\mathbf{L}(0) = \mathbf{0}$, (b) $\mathbf{L}(0) \neq \mathbf{0}$. It can be seen that in the case of no initial angular momentum \mathbf{e}_3 mainly undergoes a librational motion with a

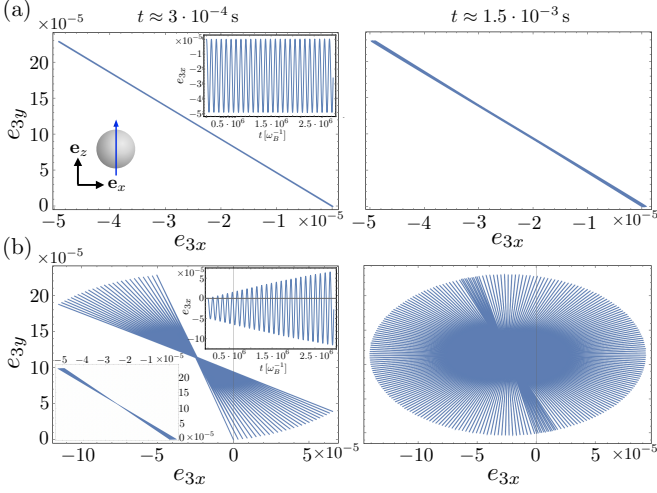


Figure 11. Dynamics of \mathbf{e}_3 in the xy plane for a sphere of size $R = 1.5 \mu\text{m}$ and a red detuned system with $P_2 = 0.02 \text{ W}$ and $P_1 = P_2/2$. The initial configuration is such that $\mathbf{S} \parallel \mathbf{e}_3 \parallel \mathbf{e}_z$ and $\mathbf{L}(0) = \mathbf{0}$ and (b) $L_z = 49/S$ which corresponds to an initial rotation frequency of $\omega_{\text{rot}}/(2\pi) \approx 750 \text{ Hz}$. The lower inset in (b) shows the dynamics corresponding to $\omega_{\text{rot}}/(2\pi) \approx 30 \text{ Hz}$.

very slow precession. If the sphere rotates initially, then the precessional motion is amplified and it becomes recognizable that the trajectory is not closed. We want to comment that we chose a higher initial rotation frequency than the one due to the Einstein-de Haas effect in order to make the influence more visible. Higher laser powers do not change the motion in the xy plane qualitatively, but increase the amplitude of the oscillations. Further we observed that in this case there is a modulation of the components of the angular momentum with the initial angular speed, which can be seen in Fig. 12. The evolution of the absolute values, however, behaves the same as in the case of $\mathbf{L}(t=0) = \mathbf{0}$, i.e. the results are the same as in Fig. 4(c,d), except that $|\mathbf{L}_{\parallel}|$ takes the constant value $L_z(t=0)$.

The cavity field dynamics is modulated by the angular motion as we show in Fig. 13 for both blue and red detuning for two different sets of laser powers. The figure depicts the time evolution of $|\delta a_1(t)| = |\bar{a}_1 - a_1(t)|$, i.e. the deviations of the higher frequency mode from its steady state. At short times, the dominant contributions are due to the optomagnonic coupling and the fast spin dynamics. We notice that the blue detuning pumping scheme leads to instabilities in the system and an exponential generation of photons that, for the considered parameters, is not compensated by decay.

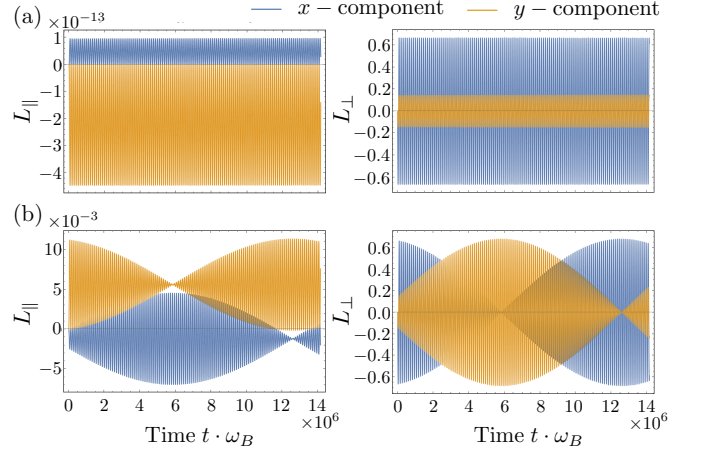


Figure 12. Dynamics of the components of the angular momentum parallel L_{\parallel} and perpendicular L_{\perp} to \mathbf{e}_3 for a sphere of size $R = 1.5 \mu\text{m}$ and a red detuned system with $P_2 = 0.02 \text{ W}$ and $P_1 = P_2/2$. The initial configuration is such that $\mathbf{S} \parallel \mathbf{e}_3 \parallel \mathbf{e}_z$ and (a) $\mathbf{L}(0) = \mathbf{0}$ and (b) $L_z = 49/S$ which corresponds to an initial rotation frequency of $\omega_{\text{rot}}/(2\pi) \approx 750 \text{ Hz}$.

Appendix F: Resonance Peak

In order to obtain the frequencies of the peaks in the power spectra analytically, we derive the eigenfrequencies of the system by linearizing the equations of motion Eq. (14) (here $\mathbf{l} = \mathbf{L}/S$, $\mathbf{s} = \mathbf{S}/S$) around the steady state and consider small oscillations around it,

$$\xi(t) = \bar{\xi} + \delta\xi(t).$$

To simplify the calculations, we assume that the steady state for the spin and the anisotropy axis is sufficiently close to the north pole, i.e. $\bar{s}_+ = \bar{e}_{3+} \approx 0$ and $\bar{s}_z = \bar{e}_{3z} \approx 1$. Further, we take a non-rotating sphere, $\bar{\mathbf{l}} = \mathbf{0}$, and denote the steady states of the optical field as $\alpha_{1,2}$. In what follows we adopt the shorthand notation $\delta\xi \equiv \xi$ and $e_{3+} = e_{3x} + ie_{3y}$, $l_+ = l_x + il_y$. Under these assumptions, we can write the linearized equations of motion as

$$\begin{aligned} \dot{e}_{3+} &= -i\omega_I S l_+, \\ \dot{l}_+ &= 2i\omega_D S (s_+ - e_{3+}), \\ \dot{s}_+ &= -i\tilde{\omega}_B s_+ - i\bar{B}_+ s_z - i\delta B_+ + 2i\omega_D S e_{3+}, \\ \dot{s}_z &= -\frac{i}{2}\bar{B}_+^* s_+ + \frac{i}{2}\bar{B}_+ s_+^*, \\ \dot{a}_1 &= \left(i\Delta_1 - \frac{\kappa}{2}\right) a_1 - igS\alpha_2 s_+ + \delta\varepsilon_1, \\ \dot{a}_2 &= \left(i\Delta_2 - \frac{\kappa}{2}\right) a_2 - igS\alpha_1 s_+^* + \delta\varepsilon_2, \end{aligned} \quad (\text{F1})$$

where we introduced $\tilde{\omega}_B = \omega_B + 2\omega_D S$ and $B_+ = 2ga_1 a_2^*$. Moving to frequency space via $\xi(\omega) = \int_{-\infty}^{\infty} e^{i\omega t} \xi(t) dt$,

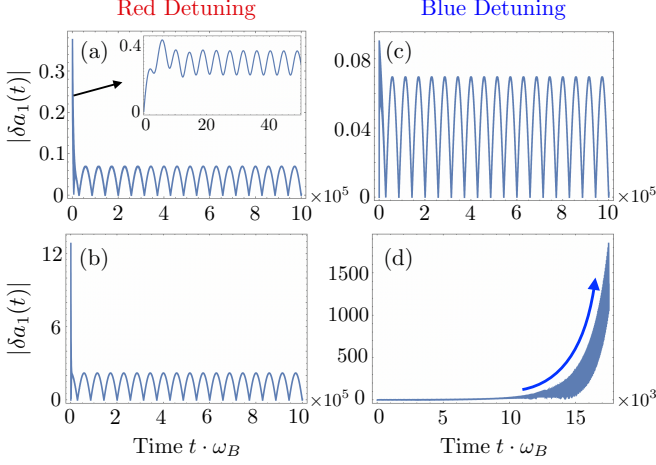


Figure 13. Dynamics of the cavity mode 1 for a sphere of size $R = 1.5 \mu\text{m}$. The plots are for both red and blue detuning schemes, and for (a,c) $P_2 = 0.02 \text{ W}$, and (b,d) $P_2 = 0.2 \text{ W}$. For both cases $P_1 = P_2/2$. The initial configuration is such that $\mathbf{S} \parallel \mathbf{e}_3 \parallel \mathbf{e}_z$. The inset of (a) shows the dynamics in the initial times evolution. After a transient period, the cavity dynamics is modulated by the dynamics of the anisotropy axis. The blue detuning scheme can lead to instabilities as shown in (d).

$\xi^*(\omega) = \int_{-\infty}^{\infty} e^{i\omega t} \xi^*(t) dt$ leads to a set of algebraic equations

$$\begin{aligned}
-i\omega e_{3+}(\omega) &= -i\omega_I S l_+(\omega), \\
-i\omega l_+(\omega) &= 2i\omega_D S (s_+(\omega) - e_{3+}(\omega)), \\
-i\omega s_+(\omega) &= -i\tilde{\omega}_B s_+(\omega) - i\bar{B}_+ s_z(\omega) \\
&\quad - 2ig(\alpha_2^* a_1(\omega) + \alpha_1 a_2^*(\omega)) + 2i\omega_D S e_{3+}(\omega), \\
-i\omega s_z(\omega) &= -\frac{i}{2}\bar{B}_+ s_+(\omega) + \frac{i}{2}\bar{B}_+ s_+^*(\omega), \\
-i\omega a_1(\omega) &= \left(i\Delta_1 - \frac{\kappa}{2}\right) a_1(\omega) - igS\alpha_2 s_+(\omega) + \delta\varepsilon_1(\omega), \\
-i\omega a_2(\omega) &= \left(i\Delta_2 - \frac{\kappa}{2}\right) a_2(\omega) - igS\alpha_1 s_+^*(\omega) + \delta\varepsilon_2(\omega),
\end{aligned} \tag{F2}$$

which we want to solve for $a_1(\omega)$. Rearranging and substituting the equations for $e_{3+}(\omega)$ and $l_+(\omega)$ into each other yields

$$e_{3+}(\omega) = \frac{2\omega_D \omega_I S^2}{2\omega_D \omega_I S^2 - \omega^2} s_+(\omega).$$

Inserting this expression and the equation for $s_z(\omega)$ into the one for $s_+(\omega)$ gives

$$\begin{aligned}
-i \left(\omega - \tilde{\omega}_B - \frac{|\bar{B}_+|^2}{2\omega} + \frac{4\omega_D^2 \omega_I S^3}{2\omega_D \omega_I S^2 - \omega^2} \right) s_+(\omega) \\
= \frac{i}{2\omega} \bar{B}_+^2 s_+^*(\omega) - 2ig(\alpha_2^* a_1(\omega) + \alpha_1 a_2^*(\omega)).
\end{aligned} \tag{F3}$$

For now we neglect the term $\propto s_+^*(\omega)$ and by defining

$$\chi_+(\omega) = \left[\omega - \tilde{\omega}_B - \frac{|\bar{B}_+|^2}{2\omega} + \frac{4\omega_D^2 \omega_I S^3}{2\omega_D \omega_I S^2 - \omega^2} \right]^{-1}, \tag{F4}$$

we get

$$s_+(\omega) = 2g\alpha_2^* \chi_+(\omega) a_1(\omega) + 2g\alpha_1 \chi_+(\omega) a_2^*(\omega). \tag{F5}$$

Substituting this expression in the equation for $a_1(\omega)$ and rearranging it yields

$$\begin{aligned}
\left[-i \left(\omega + \Delta_1 - 2g^2 S |\alpha_2|^2 \chi_+(\omega) \right) + \frac{\kappa}{2} \right] a_1(\omega) = \\
- 2ig^2 S \alpha_2 \alpha_1 \chi_+(\omega) a_2^*(\omega) + \delta\varepsilon_1(\omega),
\end{aligned} \tag{F6}$$

where again, for now, we do not consider the term $\propto a_2^*(\omega)$, such that

$$\left[-i \left(\omega + \Delta_1 - 2Sg^2 |\alpha_2|^2 \chi_+(\omega) \right) + \frac{\kappa}{2} \right] a_1(\omega) = \delta\varepsilon_1(\omega). \tag{F7}$$

The peaks of the power spectrum are then given by the zeroes of the imaginary part of the function

$$\begin{aligned}
\chi_1^{-1}(\omega) &= -i \left(\omega + \Delta_1 - 2Sg^2 |\alpha_2|^2 \chi_+(\omega) \right) + \frac{\kappa}{2} \\
&= -i(\omega + \Delta_1) + \frac{\kappa}{2} \\
&\quad - \frac{2iSg^2 |\alpha_2|^2}{\omega - \tilde{\omega}_B - \frac{|\bar{B}_+|^2}{2\omega} + \frac{4\omega_D^2 \omega_I S^3}{2\omega_D \omega_I S^2 - \omega^2}},
\end{aligned} \tag{F8}$$

and the resonance frequencies are obtained to a reasonable approximation by solving

$$\begin{aligned}
(\omega + \Delta_1) \left(\omega - \tilde{\omega}_B - \frac{|\bar{B}_+|^2}{2\omega} + \frac{4\omega_D^2 \omega_I S^3}{2\omega_D \omega_I S^2 - \omega^2} \right) \\
- 2Sg^2 |\alpha_2|^2 = 0.
\end{aligned} \tag{F9}$$

We now want to include the terms $\propto s_+^*(\omega)$ and \propto

$a_2^*(\omega)$. By inserting

$$\begin{aligned}
e_{3+}^*(\omega) &= \frac{2\omega_D\omega_I S^2}{2\omega_D\omega_I S^2 - \omega^2} s_+^*(\omega), \\
a_1^*(\omega) &= \frac{-gS\alpha_2^* \left(\omega - \Delta_1 - i\frac{\kappa}{2} \right)}{\frac{\kappa^2}{4} + (\omega - \Delta_1)^2} s_+^*(\omega) \\
&\quad + \frac{i(\omega - \Delta_1) + \frac{\kappa}{2}}{\frac{\kappa^2}{4} + (\omega - \Delta_1)^2} \delta\varepsilon_1^*(\omega), \\
a_2(\omega) &= \frac{gS\alpha_1 \left(\omega + \Delta_2 - i\frac{\kappa}{2} \right)}{\frac{\kappa^2}{4} + (\omega + \Delta_2)^2} s_+^*(\omega) \\
&\quad + \frac{i(\omega + \Delta_2) + \frac{\kappa}{2}}{\frac{\kappa^2}{4} + (\omega + \Delta_2)^2} \delta\varepsilon_2(\omega), \\
a_2^*(\omega) &= \frac{-gS\alpha_1^* \left(\omega - \Delta_2 - i\frac{\kappa}{2} \right)}{\frac{\kappa^2}{4} + (\omega - \Delta_2)^2} s_+(\omega) \\
&\quad + \frac{i(\omega - \Delta_2) + \frac{\kappa}{2}}{\frac{\kappa^2}{4} + (\omega - \Delta_2)^2} \delta\varepsilon_2^*(\omega), \tag{F10}
\end{aligned}$$

into

$$\begin{aligned}
-i\omega s_+^*(\omega) &= i\tilde{\omega}_B s_+^*(\omega) + i\bar{B}_+^* s_z(\omega) - 2i\omega_D S e_{3+}^*(\omega) \\
&\quad + 2ig(\alpha_2 a_1^*(\omega) + \alpha_1^* a_2(\omega))
\end{aligned}$$

we obtain

$$s_+^*(\omega) = \chi_-(\omega) \left[-\frac{1}{2\omega} \bar{B}_+^{*2} s_+(\omega) + C_1 \right], \tag{F11}$$

with

$$\begin{aligned}
\chi_-^{-1}(\omega) &= \left[\omega + \tilde{\omega}_B - \frac{1}{2\omega} |\bar{B}_+|^2 - \frac{4\omega_D^2 \omega_I S^3}{2\omega_D \omega_I S^2 - \omega^2} \right. \\
&\quad + \frac{2g^2 S |\alpha_1|^2 (\omega + \Delta_2 - i\frac{\kappa}{2})}{\frac{\kappa^2}{4} + (\omega + \Delta_2)^2} \\
&\quad \left. - \frac{2g^2 S |\alpha_2|^2 (\omega - \Delta_1 - i\frac{\kappa}{2})}{\frac{\kappa^2}{4} + (\omega - \Delta_1)^2} \right], \tag{F12}
\end{aligned}$$

and

$$\begin{aligned}
C_1 &= -\frac{2g\alpha_2 \left[i(\omega - \Delta_1) + \frac{\kappa}{2} \right]}{\frac{\kappa^2}{4} + (\omega - \Delta_1)^2} \delta\varepsilon_1^*(\omega) \\
&\quad - \frac{2g\alpha_1^* \left[i(\omega + \Delta_2) + \frac{\kappa}{2} \right]}{\frac{\kappa^2}{4} + (\omega + \Delta_2)^2} \delta\varepsilon_2(\omega). \tag{F13}
\end{aligned}$$

Substituting the expressions for $s_+^*(\omega)$ and $\alpha_2^*(\omega)$ in Eq. (F3) yields after some rearrangements

$$\begin{aligned}
s_+(\omega) &= \tilde{\chi}_+(\omega) \left[2g\alpha_2^* a_1(\omega) - \frac{\bar{B}_+^2}{2\omega} \chi_-(\omega) C_1 \right. \\
&\quad \left. + \frac{2g\alpha_1 \left[i(\omega - \Delta_2) + \frac{\kappa}{2} \right]}{\frac{\kappa^2}{4} + (\omega - \Delta_2)^2} \delta\varepsilon_2^*(\omega) \right], \tag{F14}
\end{aligned}$$

where

$$\begin{aligned}
\tilde{\chi}_+^{-1}(\omega) &= \left[\omega - \tilde{\omega}_B - \frac{1}{2\omega} |\bar{B}_+|^2 + \frac{4\omega_D^2 \omega_I S^3}{2\omega_D \omega_I S^2 - \omega^2} \right. \\
&\quad \left. + \frac{2g^2 S |\alpha_1|^2 (\omega - \Delta_2 - i\frac{\kappa}{2})}{\frac{\kappa^2}{4} + (\omega - \Delta_2)^2} - \frac{\bar{B}_+^2 \bar{B}_+^{*2}}{4\omega^2} \chi_-(\omega) \right]. \tag{F15}
\end{aligned}$$

With these the equation for $a_1(\omega)$ can be written as

$$\begin{aligned}
\left[-i(\omega + \Delta_1 - 2g^2 S |\alpha_2|^2 \tilde{\chi}_+(\omega)) + \frac{\kappa}{2} \right] a_1(\omega) &= \\
-2igS\alpha_2 \chi_+(\omega) C_2 + \delta\varepsilon_1(\omega), \tag{F16}
\end{aligned}$$

with

$$C_2 = -\frac{\bar{B}_+^2}{2\omega} \chi_-(\omega) C_1 + \frac{2g\alpha_1 \left[i(\omega - \Delta_2) + \frac{\kappa}{2} \right]}{\frac{\kappa^2}{4} + (\omega - \Delta_2)^2} \delta\varepsilon_2^*(\omega). \tag{F17}$$

Solving Eq. (F16) for $a_1(\omega)$ and calculating the roots of the imaginary part of the denominator yields the more precise values of the resonance peaks.

Appendix G: Details on the Cotton-Mouton Effect

The contribution of the Cotton-Mouton (CM) effect to the permittivity tensor $\varepsilon_{ij}^{\text{CM}} = \varepsilon_0 \sum_{kl} G_{ij\mu\nu} M_k M_l$ reads

$$\varepsilon^{\text{CM}} = \varepsilon_0 \begin{pmatrix} G_{11}M_x^2 + G_{12}(M_y^2 + M_z^2) & G_{44}(M_xM_y + M_yM_x) & G_{44}(M_xM_z + M_zM_x) \\ G_{44}(M_xM_y + M_yM_x) & G_{11}M_y^2 + G_{12}(M_x^2 + M_z^2) & G_{44}(M_zM_y + M_yM_z) \\ G_{44}(M_xM_z + M_zM_x) & G_{44}(M_zM_y + M_yM_z) & G_{11}M_z^2 + G_{12}(M_x^2 + M_y^2) \end{pmatrix}. \quad (\text{G1})$$

We follow the same procedure as for the Faraday effect [69], i.e. we consider a single pair of linearly polarized modes with polarization vector perpendicular to the WGM plane and perpendicular to the sphere surface, and use a spherical basis with $\mathbf{v} = \mathbf{e}_z$, $\mathbf{h} = \cos\phi\mathbf{e}_x + \sin\phi\mathbf{e}_y$, and $\mathbf{k} = \mathbf{h} \times \mathbf{v} = -\sin\phi\mathbf{e}_x + \cos\phi\mathbf{e}_y$. The electric field can then be written as $\mathbf{E} = E_v\mathbf{v} + E_h\mathbf{h}$ and the CM contribution to the electromagnetic energy is given by

$$\begin{aligned} \bar{U}_{\text{OM}}^{\text{CM}} = & \frac{1}{4}\varepsilon_0 \int \text{d}\mathbf{r} [(G_{11} - G_{12})(|E_v|^2 - |E_h|^2)M_z^2 \\ & + G_{44}(E_h^*E_v + E_v^*E_h)(M_+e^{-i\phi} + M_-e^{i\phi})M_z \\ & + M_S^2(G_{12}|E_v|^2 + G_{11}|E_h|^2)]. \end{aligned} \quad (\text{G2})$$

Here we only kept the terms which contain one factor of a transverse magnetization component $M_{\pm} = M_x \pm iM_y$ as these are relevant for one-magnon scattering processes

[103], and used $M_x^2 + M_y^2 + M_z^2 = M_S^2$. Quantizing the electric field and magnetization as before results in

$$\begin{aligned} \hat{H}_{\text{int}}^{\text{CM}} = & \hbar g_{\text{CM}}^{44} (\hat{S}_z \hat{S}_+ \hat{a}_1^\dagger \hat{a}_2 + \hat{S}_- \hat{S}_z \hat{a}_2^\dagger \hat{a}_1) \\ & + \hbar g_{\text{CM}}^{12} \hat{S}_z^2 (\hat{a}_1^\dagger \hat{a}_1 - \hat{a}_2^\dagger \hat{a}_2), \end{aligned} \quad (\text{G3})$$

where we neglected the constant shift in the photon field. The coupling constants g_{CM}^{44} and g_{CM}^{12} are given by

$$\begin{aligned} g_{\text{CM}}^{44} = & \frac{\varepsilon_0}{2\hbar} \left(\frac{M_S}{S} \right)^2 G_{44} \tilde{g}, \\ g_{\text{CM}}^{12} = & \frac{\omega_r}{8\epsilon} \left(\frac{M_S}{S} \right)^2 (G_{11} - G_{12}), \end{aligned} \quad (\text{G4})$$

under the approximation $\int \text{d}\mathbf{r} |E_h|^2 \approx \int \text{d}\mathbf{r} |E_v|^2 \approx \frac{\hbar\omega_r}{2\varepsilon_0\epsilon}$.